Journal of Structural Geology 104 (2017) 125–141

Contents lists available at ScienceDirect

Journal of Structural Geology

journal homepage: www.elsevier.com/locate/jsg

Anisotropic pore fabrics in faulted porous sandstones

N.J.C. Farrell*, D. Healy

School of Geosciences, King's College, University of Aberdeen, Aberdeen, AB24 3UE, United Kingdom

ARTICLE INFO

Article history:
Received 26 May 2017
Received in revised form
7 September 2017
Accepted 13 September 2017
Available online 22 September 2017

Keywords:
Porosity
Faulting
Image analysis
Anisotropy
Porous sandstone
Permeability

ABSTRACT

The fabric of pores in sedimentary rocks around fault zones can be subject to significant modification. Knowledge of how pore fabrics vary during and after faulting is important for understanding how rocks transmit fluids around fault zones, and can help to predict mechanical instability due to changes in pore fluid pressure. Datasets detailing the geometry of pore fabrics in faulted porous rocks are lacking. This paper describes pore fabrics quantified from two outcrops of normally faulted sandstone. The porosity and the size, shape and geometry of pores were quantified from core plugs and thin sections. Results were mapped within a framework of the faults to better illustrate how these datasets may be used to improve understanding of fluid flow around fault zones. Results from a mature, quartz-rich arenite show a change in pore fabric from pores oriented horizontally and parallel to laminations to pores oriented at a low angle to σ_1. Pore fabrics quantified from a clay-rich, quartz sub-arkose changed from moderate aspect ratio pores with no preferred orientation, to high aspect ratio pores oriented dominantly sub-parallel to the fault surface. Permeabilities measured on corresponding core plugs showed anisotropy of permeability with maximum permeability oriented down fault dip around both faults.

1. Introduction

Porosity is a measure of a rock's capacity to store fluid, and is simply defined as a scalar value equal to the ratio of the void volume to the total rock volume. Porosity is important to quantify as fluid storage capability determines the amounts of valuable resource fluids that may have accumulated. In geology, 'rock fabric' describes the organisation and geometries of crystals or grains that make up the rock and is commonly quantified to deduce the distribution of pores and interpret rock petrophysical properties such as permeability (Lucia, 1995). Although inverting the rock fabric yields summary information about the distribution of pores it fails to describe the structure and spatial organisation of the pore network, termed the 'pore fabric' in this study. Quantifying pore fabrics is essential to understand how rocks transmit fluids as this can help predict where accumulations will occur. Further to this, accommodation of fluids in pores can influence the mechanical behaviour of a material through the action of the pore fluid pressure (Hillis, 2001; Chen and Nur, 1992; Carroll, 1979; Healy, 2012). Classical permeability models represent pore populations as simplified pipes or penny-shaped cracks (e.g. Gueguen and Dienes, 1989), however advances in pore network modelling allow complex pore geometries and pore fabric anisotropy to be incorporated into fluid flow models (Blunt, 2001) and geomechanical models (Healy, 2012; Farrell, 2016 *unpublished PhD thesis*). However, despite the advent of high resolution X-ray computerized tomography (CT) - facilitating direct imaging of thousands of pores in 3D at micrometer scale - there remains a lack of statistically significant datasets quantifying pore geometries and pore fabrics of reservoir rocks within a geological context i.e. within bedded or laminated sandstone or around fault zones. Previous studies modelling fluid flow have produced large datasets detailing pore networks of fractures (Schild et al., 2000; Takemura et al, 2003) – but little or no pore fabric information has been quantified from volumetrically significant intergranular porosity. In granular rocks like sandstones, where intergranular pores make up 98% of porosity, this must be addressed.

In this study both porosity and pore fabrics have been quantified from outcrop samples of unfaulted and faulted sandstones collected from two distinct normal fault zones. These faults are hosted in common reservoir sandstone lithologies: a 'clean' aeolian quartz-rich arenite and a 'muddy' fluvial quartz sub-arkose, with distinctive mineralogies and depositional histories. Additional information on the fluid flow properties around these faults was also quantified to investigate the influence of pore fabrics on the magnitude and anisotropy of permeability.

* Corresponding author.
E-mail address: natalie.farrell@abdn.ac.uk (N.J.C. Farrell).

https://doi.org/10.1016/j.jsg.2017.09.010

1.1. Previous studies quantifying pore space in sandstones

Pore network models in granular porous media represent void space with a 2D or 3D lattice of spherical or cylindrical pores connected by narrower throats (Bryntesson, 2002). Improvements in pore space modelling can now represent complex pore geometries creating angular pores defined by grain boundaries capturing the macroscopic properties of rock in detail (Blunt, 2001; Al-Gharbi and Blunt, 2005). Datasets required to populate these models can be generated synthetically using pore network modelling or directly from natural samples using either X-ray computerized tomography (XCT) or 2D thin section images which can then be 'scaled' to 3D using stereology or multiple point statistics (Okabe and Blunt, 2004). Commonly pore network models are generated from data collected directly from natural samples, with pore geometries determined from the analysis of the solid phase i.e. grains and cements, using inverse functions to calculate the pore fabrics (Bakke and Øren, 1997). Conclusions from these studies are generally based on visual inspection of the reconstructed microstructure and with qualitative analysis of the connectivity of the pore space as a whole rather than quantification of the pore fabric.

Direct quantification of sandstone pore fabrics through analysis of thin section or XCT images is also understudied (Ruzyla, 1986; Anselmetti et al., 1998; Balsamo et al., 2009; Schmitt et al., 2016). The majority of studies calculating sandstone pore properties use indirect methods such as Mercury Injection Porosimetry (MIP) (Pittman, 1992), acoustic wave velocities (Raymer et al., 1980; Robion et al., 2014) or anisotropy of electrical responses or magnetic susceptibility (Grattoni and Dawe, 1994; Benson et al., 2003; Louis et al., 2003). Although these methods can quickly generate large datasets in comparison to direct image analysis, the primary disadvantages of indirectly analysing pore fabric are that the pores cannot be counted and the location of features within a sample is not possible. Without quantifying these details, the geometrical attributes and spatial distributions of individual pores cannot be characterised, therefore datasets cannot be fully integrated into fluid flow and geomechanical models. Incorporation of pore properties such as pore aspect ratios and pore orientations facilitates porosity quantification into the form of second, or higher, rank tensors (e.g. Oda, 1982) that can then be empirically linked to other tensorial properties such as permeability (Farrell et al., 2014), seismic velocities (Kuster and Toksöz, 1974), as well as geomechanical properties such as the elastic moduli and even strength (Zhang and Bentley, 2003; Bubeck et al., 2017; Griffiths et al., 2017).

Advances in technologies developed to quantify microstructures – whether indirectly with the methods discussed or directly using high resolution XCT – have created non-destructive techniques which define internal features and become powerful tools for evaluating rock microstructure (Mees et al., 2003). However awareness and availability of these methods to geologists has also produced a notion that – to be notable - microstructural studies of faulted and fractured rock must include something visually or methodologically novel. Studies which present innovative techniques and images can be pioneering but - as discussed - commonly present singular observations or small datasets which are not substantial enough for integration with fluid flow or geomechanical models. To progress the applicability of microstructural data to fluid flow and mechanical behaviour of faulted and fractured rock, studies are needed that systematically quantify pore fabric from interesting rocks and/or settings and produce detailed datasets that can be linked to other laboratory derived rock properties and used in predictive models.

1.2. Effects of porosity on the behaviour of rocks in the subsurface

Much previous work has focused on the influence of pore attributes and pore fabrics on fluid flow and has established a link between the connectivity of pores and the magnitude of permeability (Ehrlich et al., 1984; Walsh and Brace, 1984; Etris et al., 1988; David et al., 1994; Blair et al., 1996; Saar and Manga, 1999; Schild et al., 2000; Keehm et al., 2001; Balsamo et al., 2009; Farrell et al., 2014; Farquharson et al., 2015; Colombier et al., 2017). In porous sedimentary rocks, fault-related deformation via cataclasis reduces grain size and porosity and often reduces permeability (Pittman, 1981; Chester and Logan, 1986; Zhu and Wong, 1997). Further to this, the presence of deformation bands formed by strain localisation can create high permeability contrasts within sandstones (Manzocchi et al., 1998; Shipton et al., 2005; Torabi and Fossen, 2009). However, some studies of faulted sandstone have shown increased permeability, and/or anisotropy of permeability, linked to the development of structural features with well-connected pore types forming localised fluid flow pathways (Antonellini and Aydin, 1994; Caine et al., 1996; Farrell et al., 2014).

In contrast relatively few studies consider the impact of pore attributes and pore fabrics on the strength or geomechanical behaviour of rocks (but see, Dunn et al., 1973; Oda et al., 1985; Healy, 2012; Bubeck et al., 2017; Davis et al., 2017). Laboratory rock deformation studies have shown that fault stability is affected by fault zone architecture – i.e. the influence of gouge (Byerlee, 1967; Scholz et al., 1972; Byerlee and Summers, 1976), fault rock mineralogy (Shimamoto and Logan, 1981) and fault rock grain size (Dieterich, 1981; Biegel et al., 1989). However, there are fewer studies considering the effects of fault rock porosity on fault stability (Youd, 1972; Marone and Scholz, 1989). This may be due to a lack of information about pore fabrics in fault rocks. No study to date, on experimentally or naturally faulted rocks, has incorporated the pore properties of aspect ratio and orientations into geomechanical models.

1.3. Porosity in unfaulted sandstones

The initial control on porosity in siliciclastic rocks is the mode of deposition (Glennie et al., 1978). Porosity variations tend to be facies controlled e.g. cross-bedded sandstones may be more porous than planar-bedded sandstone, and graded bedding may have a more uniform porosity than slumped sandstone facies. These sedimentary structures are common to particular sedimentary environments; therefore the initial porosity of the rock can sometimes be predicted (Lindquist, 1988). Post-depositional diagenetic processes such as compaction and precipitation of cements from mineralising fluids can also alter porosity reducing pore volume through pressure solution (Taylor, 1950; Bernabe et al., 1992; Fisher et al., 1999; Paxton et al., 2002) and overgrowth of quartz cements respectively (McBride, 1989; McBride et al., 1995; Lander et al., 2008).

1.4. How does deformation change the sandstone pore fabric?

Microstructural studies have shown that deformation processes associated with faulting can change the size and shapes of grains in a sandstone protolith through mechanisms of compaction, cataclasis and pressure solution (Pittman, 1981; Aydin and Johnson, 1978; Blenkinsop, 1991; Antonellini et al., 1994; Fowles and Burley, 1994; Johansen et al., 2005; Torabi and Fossen, 2009; Menendez et al., 1996; Baud et al., 2004). Cementation has also been shown to increase with reducing grain size (i.e. due to grain crushing and/or cataclasis during faulting) as quartz grains can be packed closer and there is more surface area of fresh quartz for

cements to nucleate on (Reed and Laubach, 1996). Factors that influence the relative contribution of these deformation mechanisms are fault displacement, fault kinematics, depth of faulting, pore fluid pressure and chemistry. Textural studies of faulted sandstone have examined the relationship between fault depth and grain size, showing that grain size becomes smaller at greater fault depths with increasing confining pressure (Engelder, 1974; Sammis et al., 1987). These studies recognise that grain structure alteration during faulting also changes the amount of porosity and size distribution of pores (Shipton and Cowie, 2001). However, direct quantification of geometrical pore attributes such as pore aspect ratio and long axis orientation in faulted sandstones remains limited (Pittman, 1981; Schmitt et al., 2016).

Our analysis of previously published work suggests that scope exists to map and quantify brittle pore fabrics in a geological setting. This study presents quantified pore fabrics from two mineralogically distinct sandstones in unfaulted and faulted samples and uses these datasets to investigate variations in permeability. Results are interpreted in terms of the processes which form the original unfaulted porosity *and* the deformation processes which alter the porosity, and we assess whether the controls on pore fabric evolution with faulting are the same in the two different sandstones. We show that the classification of pore fabrics from the microscopic analysis of unfaulted and faulted sandstones can provide a more accurate basis for describing and understanding the controls on fluid flow around faults. Using these results, criteria can be established whereby the fault deformation processes that alter porosity might be inferred around other examples of normal faults hosted in porous sandstone.

2. Materials

Sandstone samples were collected from two outcrop examples of seismic-scale normal faults with the aim of quantifying the microstructure within faulted porous rock. The two sandstone formations had differing host rock sedimentology and cementation so that we could consider the influence of original facies and diagenesis on the *in-situ*, post-faulting porosity. Changes in grain size, mineralogy, cementation, porosity and pore geometries with progressive fault deformation were documented and interpreted through their location with respect to the fault surface and along fault strike. Changes in pore fabrics have been related to the deformation mechanisms and localisation of deformation is considered in the context of distance to the fault and the original host rock structure. By quantifying these microstructural properties in a spatial framework around the fault and in the context of the sandstone facies, our results can be used to infer pore fabric patterns around other sandstone-hosted normal faults.

2.1. Sample localities

2.1.1. Arenites around the clashach fault

High porosity, quartz-rich arenites of the Hopeman Sandstone Formation were sampled from two sites around the Clashach Fault (Scotland, UK): one from the approximate centre of the fault in cliff outcrops around a cove, and from 400 m east of the fault centre near the fault tip in an adjacent open quarry (OS grid reference, NJ159701) (Fig. 1a). The Clashach Fault comprises a narrow fault core with a well-defined, dominant slip surface and associated units of fault breccia and ultracataclasite surrounded by a zone of intensely fractured sandstone and cataclasites. Kinematic indicators included slickenlines plunging between 70° and 83°West indicating extensional movement with a small component of strike-slip and a displacement around 50 m.

The Hopeman Sandstone Formation (HSF) is a pale yellow, fine to medium grained, quartz-rich arenite deposited as aeolian cross-bedded dunes. Grains were well-sorted and loosely packed with diameters between 250 and 400 μm (Fig. 1b). Samples were compositionally mature and mineralogy was dominated by quartz grains (92%) (labelled Qtz on Fig. 1), with low K-feldspar (K-Fs) content of 7% and <1% lithics. Unfaulted HSF porosity mainly comprised large intergranular pores with highly convoluted, convex shapes made up of curved edges (Fig. 1c). Unfaulted arenites were also sampled from a highly cemented location around the fault tip where the perimeters of intergranular pores were more angular due to overgrowth of quartz cements (Qtz-Og) (Fig. 1e). In the field, the depositional grain structure of the protolith is visible as sedimentary laminations up to 50 cm to the fault surface where the original grain organisation has been destroyed via grain reshuffling and cataclasis. Faulted HSF samples were identified as visually homogenous, well-cemented sandstones with few localised deformation bands. These rocks were commonly dark to pale red colour, due to iron staining related to fluid flow around the fault core and along some localised deformation bands. Optical microscopy showed a reduction in mean grain diameters to 200–300 μm (Fig. 1d). Mineral composition continued to be dominated by quartz grains; however the percentage of feldspar grains was reduced in faulted samples as K-feldspar grains were fractured and dissolved during faulting, creating large secondary dissolution pores containing traces of authigenic kaolinite (Kln) identified using XRD analysis (Fig. 1d). Intergranular porosity was greatly reduced in faulted samples as grains became more densely packed and quartz grains were pervasively overgrown by bands of quartz cement (Fig. 1e).

2.1.2. Arkoses around the north scapa fault

The North Scapa Fault is a basin scale fault (displacement > 100 m) and juxtaposes fluvial porous sandstones against lacustrine mudstones (Hippler, 1993). Moderate porosity, fluvial quartz sub-arkoses of the Scapa Sandstone Formation were sampled at a single site from the hanging wall of the North Scapa Fault which outcrops in cliff sections and a wave-cut platform along a beach section at Orphir Bay (Orkney UK) (HY334042) (Fig. 2a). The sandstones hosting these faults are similar to hydrocarbon-bearing reservoirs in the North Sea.

The Scapa Sandstone Formation (SSF) is a pale cream, fine grained, quartz sub-arkose deposited as cross-bedding in a principally fluvial environment. Arkoses were well-sorted with a mean grain diameter around 200 μm (Fig. 2b). Grains were closely packed with pressure solution observed at grain contacts and extensive quartz cements overgrown around groups of grains (Fig. 2c). Unfaulted SSF was dominated by quartz grains (labelled Qtz on Fig. 2) however these sandstones were not as mature as the quartz-rich arenites and this was reflected in a mineralogy comprising quartz (80%) with a larger proportion of 'weaker' minerals including K-feldspar (K-Fs) (14%), kaolinite (Kln) (5%) and mica (<1%). SSF porosity was bimodal comprising large, oblate pores with jagged/frayed outlines termed 'macro' pores and clusters of very small pores surrounded by authigenic kaolinite termed 'micro' pores (Fig. 2c). Larger oblate pores were spatially distributed and visually unconnected.

In the field, faulted SSF samples retained a pale cream colour and sedimentary lamination was visible in fractured rocks >10 m from the fault surface. Faulted arkoses were characterised by extensive macrofractures including shear fractures, joints and thin bitumen stained, tensile fractures. Mean grain size were reduced by grain comminution to very fine to fine grained (100–200 μm) (Fig. 2d). Faulted arkose compositions were dominated by quartz grains with an increased percentage of authigenic kaolinite produced after deformation and dissolution of K-feldspar grains

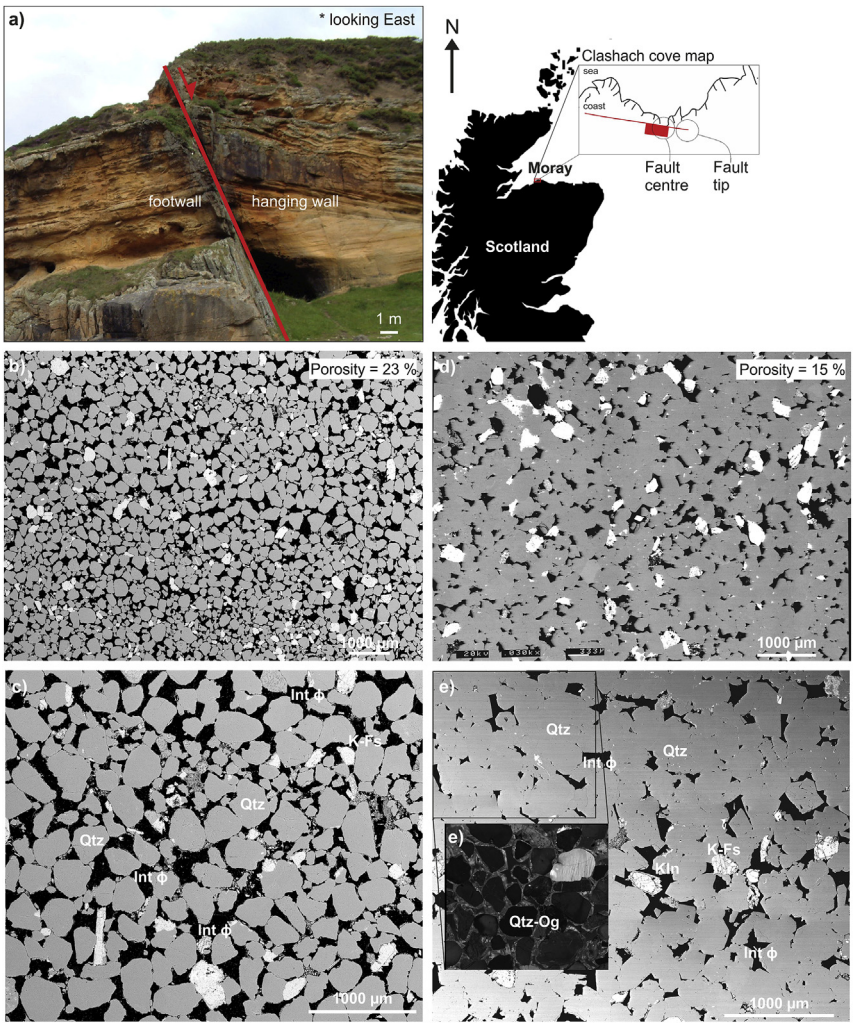

Fig. 1. (a) The Clashach Fault on the Moray Coast (Scotland) a normal fault with around 50 m displacement hosted in aeolian, quartz-rich arenite. The inset diagram shows the locality of the outcrop. SEM-BSE images showing grain, pore and matrix properties of samples from (b, c) unfaulted aeolian, quartz-rich arenites from the Hopeman Sandstone Formation (HSF) and from (d, e) faulted HSF arenites sampled close to the Clashach Fault. Grains are labelled as quartz (Qtz), K-feldspar (K-Fs). Porosity is labelled as, intergranular porosity (Int phi).

(Fig. 2e). Faulted SSF porosity was also bimodal comprising macro and micro porosity.

2.2. Sample preparation

Oriented blocks (approx. 20 × 20 × 20 cm) were collected at a range of distances from the fault surface, in the faulted rocks and the unfaulted protolith (Fig. 3a). At the Clashach Fault a total of 26 arenite samples were taken from the hanging wall and footwall of the fault. At the North Scapa Fault, 19 arkose samples were taken from the continuously exposed hanging wall. Samples were spaced at ~5 m intervals. The majority of samples were collected from the same facies type (aeolian dune facies in the arenite, and cross-bedded fluvial facies in the arkose) so that each sample set can be assumed to have comparable original grain sizes and associated host rock petrophysical properties. Facies types were checked in faulted samples by tracing sampled units away from the fault surface to locations where the original facies were assessed through sedimentary logging.

In the laboratory, samples were re-oriented to match field orientations and cored in three perpendicular orientations: normal to the fault (x), along fault strike (y) and parallel to fault dip (z) (Fig. 3b). Where possible, multiple samples were cored in a single direction. Core plug dimensions are 2.54 cm in diameter with varying lengths between 2.54 and 5.08 cm. Eighty-eight arenite core plugs and sixty-three arkose core plugs were made. Due to variable success with coring samples, full sets of 3 perpendicular core plugs were produced from 12 arenite samples and 15 arkose samples. Thin sections were made from samples mostly corresponding to the ends of core plugs. SEM-BSE (Scanning Electron Microscope, Back-Scattered Electron) - images of thin sections were produced and pore geometries were quantified from 13 arenite and 13 arkose thin sections. The geometry of pores in xz thin sections were used to investigate how the deformation of normal faulting changed the pore fabric.

3. Methodology: imaging and characterising porosity

Volume porosity was quantified from core plug samples and 2D pore geometries were quantified from high resolution thin section images. To reduce sampling error image areas over 100 times larger than the average pore size were used. Images of entire thin sections

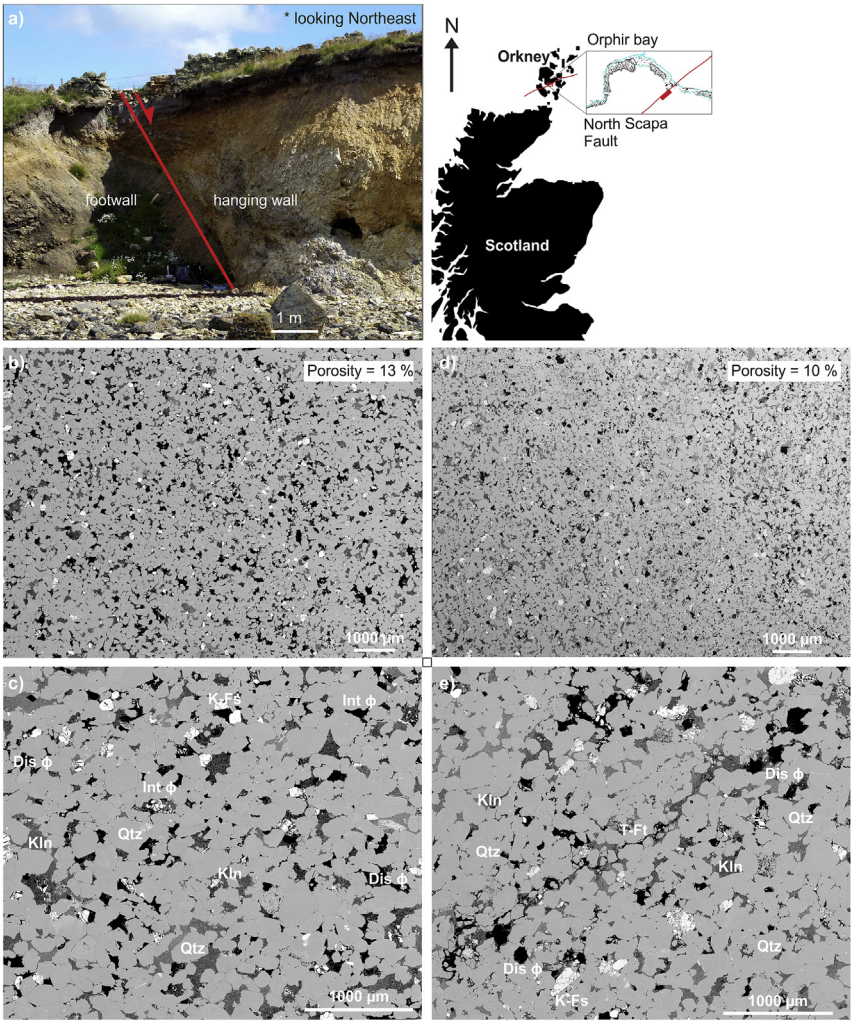

Fig. 2. (a) The North Scapa Fault on Mainland Orkney is a normal fault with over 100 m displacement, hosted in a fluvial, quartz sub-arkose. SEM-BSE images showing grain, pore and matrix properties of samples from (b, c) the unfaulted fluvial, quartz sub-arkoses from the Scapa Sandstone Formation (SSF) and from (d, e) faulted SSF arkoses sampled close to the North Scapa Fault. Grains are labelled as quartz (Qtz), K-feldspar (K-Fs), kaolinite (Kln). Porosity is labelled as, intergranular pore (Int phi), secondary dissolution pore (Dis phi), transgranular fracture (T-Ft).

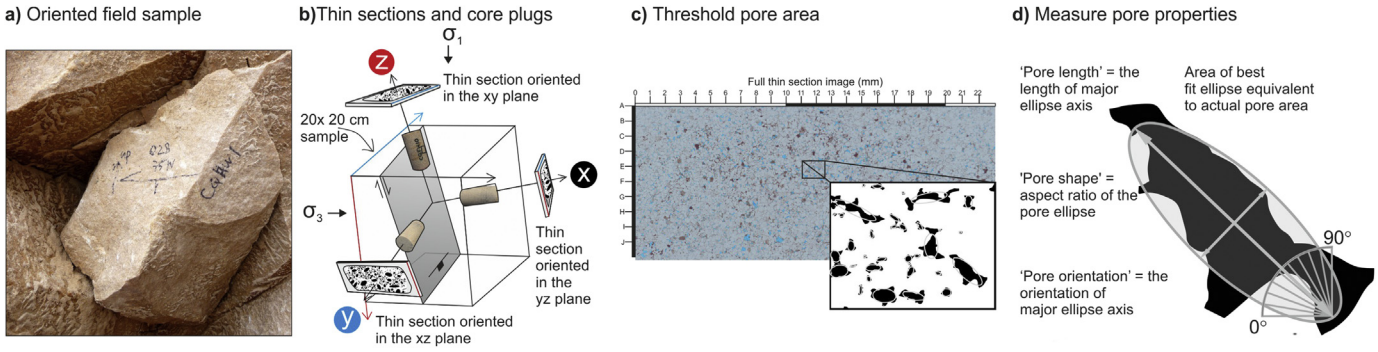

Fig. 3. Field samples were reoriented in the context of the fault orientation before (a) thin sectioning and (b) core plugging. Thin sections with porosity highlighted by blue epoxy were thresholded to produce binary images (c) showing grains (white) and porosity (black). Pore shapes were simplified using a best-fit ellipse. Ellipse geometries were characterised by (d) pore area, axis lengths, aspect ratio and major axis orientation. (For interpretation of the references to colour in this figure legend, the reader is referred to the web version of this article.)

were used in samples where pores were easily thresholded under optical microscopy and montaged BSE images were used where pores were too small to image with a slide scanner or pore boundaries were occluded with kaolinites.

3.1. Measuring porosity

Connected porosity was measured using a helium porosimeter at room temperature. Core plugs were put into a tight compartment

and a known volume of He gas was injected from a separate chamber at 100 psi. The resulting lower pressure in the core plug chamber was recorded and then an equilibrium pressure of the two chambers was calculated. An expression of Boyle's Law – which assumes that gas pressures have a positive correlation to gas volumes – was used to calculate grain volume. Porosity was then derived from the core plug grain volume subtracted from the bulk volume - calculated from the caliper dimensions and density of the core plug.

3.2. Identifying pore types

Pore types were identified from SEM-BSE images and determined using pre-existing pore type classifications i.e. intergranular pores, grain dissolution pores (Pittman, 1981). The area covered by each pore type was thresholded and defined as a percentage of the total porosity.

Microstructural characterisation of arkoses showed that a significant amount of porosity in unfaulted and faulted samples was occluded by authigenic kaolinite (Fig. 2c and e). To investigate the role of pore fabric on permeability anisotropy the pore properties of in-situ porosity - where pore fluids will reside – were quantified. However kaolinite filled pores were shown to contain a significant amount of microporosity, which in saturated conditions would contain fluids. Also because kaolinite clays occur as discrete platy particles they have previously be shown to have minimal impact on permeability compared to pore lining clays like illite and chlorite (Neasham, 1977). Therefore in the analysis of arkose pore geometry attributes were defined for in-situ pores (black in BSE images) and in-situ pores plus kaolinite filled pores, with perimeters defined by the grains bounding the kaolinite (Fig. 2c and e).

3.3. Measuring pore shape

Thin section images were turned into binary images so that black pores could be easily thresholded. Pore properties were quantified in image analysis software, ImageJ (Schneider et al., 2012) using a region based, best-fit ellipse algorithm (Kang et al., 2012). This method replaced an irregularly shaped pore with an ellipse with the same area, orientation and centroid as the original selection (Fig. 3c). Quality tests confirmed that the total area of fitted ellipses matched the pore area provided by the original image. Using this method the properties of up to 10,000 pores were automatically quantified from a single thin section. A pore length cut-off of <10 μm was applied to images as the number of pixels used to image these pores on a 4000 dpi full thin section image was too small to define accurate aspect ratios.

Analysis of pore ellipse geometries was carried out to assess the pore property distributions and define statistically representative pore geometries for each thin section. Pore geometry analysis was conducted on 13 arenite thin section images and 13 arkose thin section images. Pore types were combined to quantify the overall in-situ pore property distributions in each thin section. Four pore properties; area, diameter, aspect ratio and long-axis orientation were quantified from each individual pore ellipse (between 2500 and 10,000 pores quantified per thin section) (Fig. 3d). Pore properties from thin sections corresponding to the ends of y - oriented core plugs (e.g. xz plane and normal to along fault strike) were plotted against distance to the fault plane. The y orientation was chosen as - in the framework of an Andersonian normal fault - this plane is a cross section where the stress ratio between vertical and horizontal stresses is greatest, therefore deformation features are likely to be most pronounced (Fig. 3b). To fully illustrate the spread of data, boxplots have been used which display five standard sample statistics (maximum and minimum values, upper and lower quartiles and mean) as well as values which exceed twice the interquartile range classed as 'outliers'. As with many natural phenomena, pore sizes are not normally distributed and mode pore lengths quantified in this study were often the same value as the minimum. The aim of this study was to investigate the influence of pore fabrics on permeability hence our interest was in pores that contributed the most to pore area and dominated the pore fabric as they are likely to conduct the most fluid. Therefore - as well as quantifying pore property distributions - mean pore lengths ($d_{corrected}$) were calculated (binned by increments of 100 μm for arenite and 5 μm for arkose) weighted by the pore area (A) i.e.

$$d_{corrected} = \frac{\sum (A_i d_i)}{\sum A_i} \quad (1)$$

3.4. Permeability

Permeabilities were measured using the steady state, constant flowrate method on a Jones permeameter at 2.7 MPa confining pressure, with nitrogen as the permeant. Tests were run at room temperatures, 18–20 °C. Permeability was calculated using a modified Darcy equation – which normalises changes in pressure by mean pressure – expressed as:

$$K = 2\mu Q \left(\frac{L}{A}\right) \Big/ \left(P_1^2\right) - \left(P_2^2\right) \quad (2)$$

where K = permeability (millidarcies, mD), μ = viscosity (centipoise, cP), Q = gas flow rate calculated from V/t, volume of fluid (cm^3) passed in time (s^{-1}), L and A = core plug length and cross-sectional area (cm and cm^2), P_1 and P_2 are the input pressure and output pressure respectively (atmospheres). An average gas pressure (P_{mean}) was calculated for each core plug from a range of input and output pressures. Measured permeability (mD) was then plotted against $1/P_{mean}$ (1/atm) with a line of 'best-fit'. Permeabilities with 'best-fit' correlation coefficients (R_2) < 0.9 were repeated. The intersection of the plotted line with the y axis (permeability) gives the permeability of the core plug with an applied Klinkenberg correction. The Klinkenberg correction allows gas permeability measurements to be 'corrected' to the permeability of a core with a liquid flowing through it (Klinkenberg, 1941).

4. Results

To consider how unfaulted protolith pore properties influenced pore fabric development (relative to fault deformation style and magnitude controls) the pore properties of unfaulted arenites and arkoses were quantified as well as faulted samples. This section characterises the pore fabrics of unfaulted and faulted sandstones by describing their varying porosities (Section 4.1), pore types (4.2) and pore shapes (4.3). To consider the role these pore fabrics have on controlling fluid flow around faults, corresponding permeabilities of arenites and arkoses are also presented (Section 4.4).

4.1. Porosity

4.1.1. Arenite

Porosities of connected pores were measured from 88 core plugs made from arenites collected around the Clashach Fault (Section 2.2). Mean porosities decreased in the hanging wall and footwall towards the fault surface, from ~22% in the unfaulted, uncemented protolith to 12.3% porosity in cataclasites and 14% in ultra-cataclasites of the fault damage zone and core respectively (Fig. 4).

Unfaulted arenites were relatively homogeneous with poorly consolidated arenites from the fault centre showing porosities between 20% and 25%. Porosities of unfaulted, quartz cemented arenites sampled around the fault tip ranged between 12% and 14%. Faulted arenite porosities in the damage zone showed more variation and ranged broadly between 8% and 20%. Fault core porosities were also heterogeneous and showed the widest range in porosities between 7% and 22%.

4.1.2. Arkose

Helium porosities were measured from 63 core plugs made from arkoses collected from the hanging wall of the North Scapa Fault. Overall mean porosities were reduced closer to the fault surface, from 11.8% in the unfaulted protolith and 11.7% in the fractured outer damage zone, to 9.5% in the intensely fractured and cataclased inner damage zone samples (Fig. 5). Cores could not be made from the fault core as the samples were too fractured to be cored. Maximum porosities were identified in the outer damage zone where the majority of porosities were >11%. In contrast porosities from the inner damage zone cataclasites (<10 m from the fault surface) were generally < 10%.

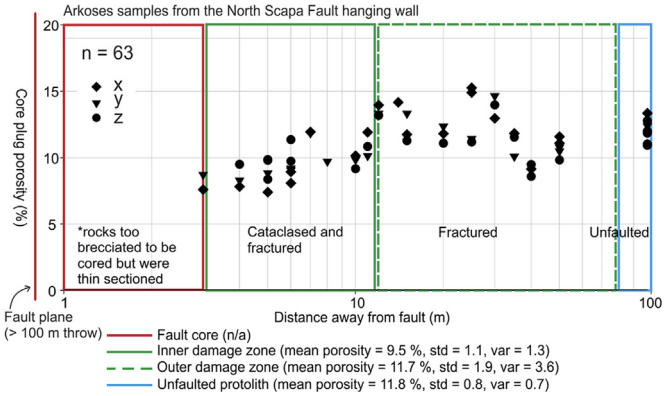

Fig. 5. Graph showing changes in arkose porosity with distance to the fault surface. Porosities measured from core plugs increased in the outer damage zone due to fracturing and decreased with cataclasis in the inner damage zone. Cores were sampled in three orientations. Porosities measured in core plugs from a single sample tended to be relatively homogeneous.

4.2. Pore types

A thresholding and image analysis technique was used calculate the pore area contribution of different pore types in samples taken at varying distance to the fault surfaces (Section 3.2).

4.2.1. Arenite

Four main pores types were identified from 15 thin sections of faulted arenite and 1 thin section of unfaulted arenite. Pore types included intergranular pores (labelled Int Φ) (Fig. 6a), grain dissolution pores (Dis Φ) (Fig. 6b), intragranular fracture pores (Ft Φ) (Fig. 6c) and transgranular fracture pores (T-Ft Φ) (Fig. 6d). Although 2D pore area is not representative of 3D pore volume, total pore areas quantified from BSE images of arenite thin sections (shown by the total bar height) showed a decreasing trend towards the Clashach Fault surface (Fig. 6e), similar to that shown by core plugs.

Relative pore type contributions showed that most samples of faulted and unfaulted arenite were dominated by intergranular pores (Fig. 6e). The remaining pore area was made up of dissolution pores, while transgranular and intergranular fractures were grouped and typically contributed <5% of total pore area. Intergranular pores in faulted arenites tended to have a basic, angular and concave outline with moderate aspect ratios and a size range from around 100 to 500 μm (Fig. 6a). Dissolution pores formed by the deformation and dissolution of K-feldspar grains were identified by traces of authigenic kaolinite remnant in the pores. Dissolution pores were present in some faulted samples and – where present - contributed a large amount to pore area; however these pores were relatively isotropic with low aspect ratios and were often visually poorly connected to the rest of the pore fabric (Fig. 6b). Fracture porosity generated during faulting was observed as few intragranular tensile fractures (Fig. 6d).

4.2.2. Arkose

Four main pore types were identified from 16 thin sections of faulted arkose and 3 thin sections of unfaulted arkose. Pore types included: intergranular pores (Int Φ), grain dissolution pores (Dis Φ), intragranular fracture pores (Ft Φ) and transgranular fracture pores (T-Ft Φ) (Fig. 7a – d respectively). Intergranular pores in faulted arkose samples had convoluted outlines with high aspect ratios and a broad size range from 100 to >1000 μm. Many large intergranular pores were partially occluded with authigenic kaolinite (Fig. 7a). Dissolution pores were common in unfaulted and faulted arkoses. These pores had simple shapes with low aspect ratios; as well as long thin shapes with high aspect ratios (Fig. 7b). Intragranular fractures in faulted arkoses were mostly present in K-feldspar grains which were weaker and tended to fracture more easily (Fig. 7c). Large transgranular fractures were common in

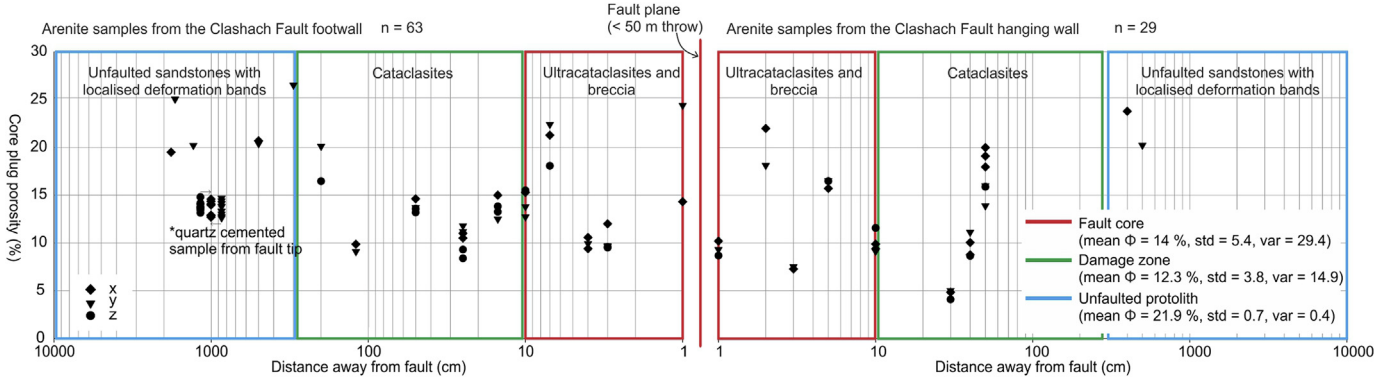

Fig. 4. Graphs showing changes in arenite porosity with distance to the fault surface. Porosities measured from core plugs decreased in the footwall and hanging wall with increased deformation (i.e. closer to the fault surface). Cores were sampled in three orientations (x, y and z). Porosities measured in core plugs from a single sample were relatively homogeneous, therefore core plug orientation does not affect the magnitude of porosity.

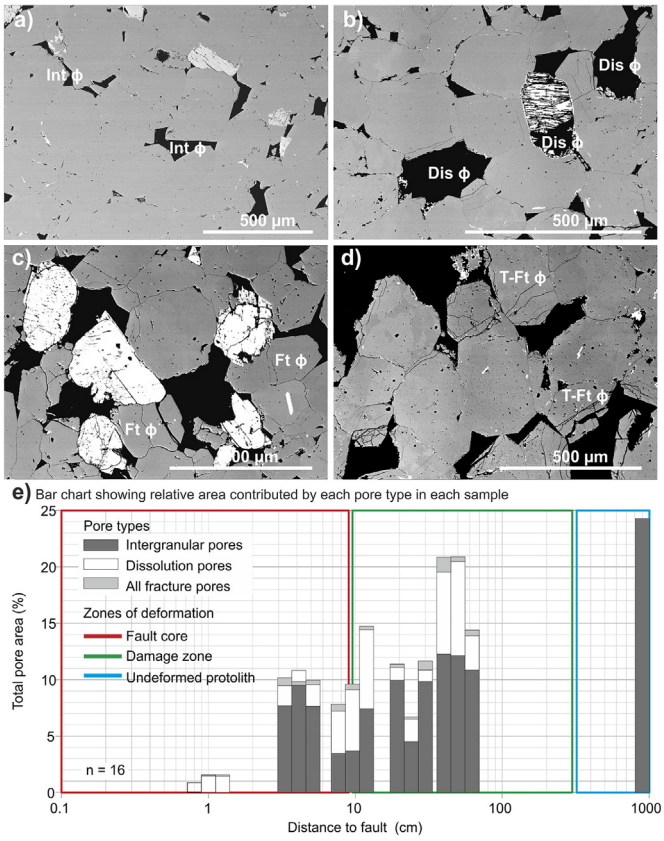

Fig. 6. SEM-BSE images showing different pore types identified from arenites collected around the Clashach Fault. Pore types quantified include: (a) intergranular porosity (Int ϕ), (b) secondary dissolution porosity (Dis ϕ), (c) fracture porosity (Ft ϕ) and (d) transgranular fracture porosity (T-Ft ϕ). The area covered by each pore type was thresholded from a montage of SEM-BSE images (3.5 mm × 4 mm) and defined as a percentage of the total image area. A Bar chart (e) depicts the pore area distributions in each arenite sample collected around the Clashach Fault. See Fig. 1c and e for constituting minerals in (a)–(d).

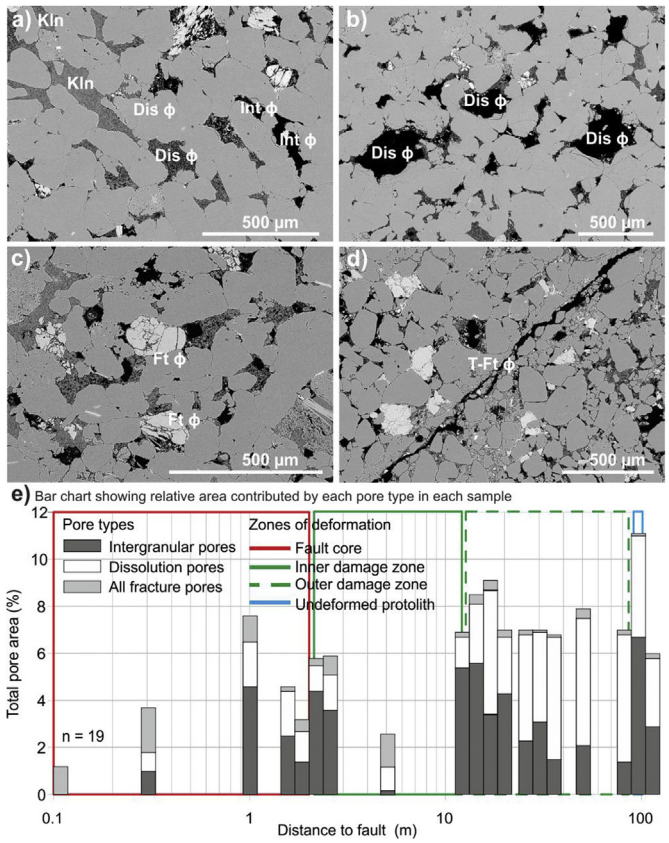

Fig. 7. Pore types identified from SEM-BSE images of quartz sub-arkoses collected around the North Scapa Fault including (a) intergranular porosity, (Int φ) and porosity filled by kaolinite (Kln), (b) secondary dissolution porosity (Dis φ), (c) intragranular fracture porosity (Ft φ) and (d) transgranular fractures (T-Ft φ). The area covered by each pore type was thresholded from a montage of SEM-BSE images (3.5 mm × 4 mm) and defined as a percentage of the total image area. A Bar chart (e) depicts the pore area distributions in each arkose sample collected around the North Scapa Fault. See Fig. 2c and e for constituting minerals in (a)–(d).

highly faulted samples <10 m from the fault surface where they were often the dominant porosity type present (Fig. 7e). These fractures were commonly over 3000 μm in length with widths of <50 μm giving them very high aspect ratios (Fig. 7d).

In correlation with porosity patterns quantified from core plugs (Fig. 5), pore areas quantified from faulted arkoses in the inner damage zone were lower than pore areas of unfaulted arkoses and faulted arkoses from the outer damage zone. Apportion of pore area by pore type showed a corresponding decrease in dissolution porosity from between 3 and 5% in the protolith and outer damage zone to <2% in the inner damage zone and fault core (Fig. 7e). In contrast fracture pore area was higher in the inner damage zone compared to arkoses from the outer damage zone. Results showed that although deformation simplified the perimeters of intergranular pores (Fig. 7a); their contribution to pore area is similarly variable in unfaulted and faulted arkoses (Fig. 7e).

4.3. Pore shape

Pore geometry analysis was conducted on 13 y – oriented, thin section images of arenite and 13 arkose images. Pore types were combined to quantify the overall in-situ pore property distributions in each thin section. Four pore properties; area, length, aspect ratio and long-axis orientation quantified from individual pore ellipses are illustrated and described in the following sections.

4.3.1. Arenite

Arenites were sampled from two localities along the fault strike; in the centre of the fault and 400 m away at the fault tip (Fig. 1). The protolith was variable between localities with unconsolidated, high porosity arenites at the fault centre and quartz cemented, lower porosity arenites at the fault tip (Fig. 4). In this section results were divided by sampling location to examine the effects of varying along strike fault behaviour and variable cementation on the development of fault rock pore fabrics.

Pore size was quantified using pore length (Fig. 3d). Results showed that as arenites were increasingly deformed closer to the Clashach Fault the total range of pore lengths quantified within single samples reduced (Fig. 8). Fault centre pore lengths decreased from a broad range (15 to > 4000 μm) in unfaulted protolith to a narrower range of smaller pores (10–~1500 μm) in damage zone cataclasites and in fault core ultracataclasites (20–~800 μm) (Fig. 8a). Notably interquartile ranges (marked by the box top and bottom) were lowest in the damage zone and showed a non-linear increase in the fault core. Pore mean lengths - weighted by area (illustrated by a red star) - decreased by an order of magnitude from 1500 μm to 200 μm closer to the fault surface (Fig. 8a). Fault tip arenites showed a moderate range of pore lengths (10 μm–1500 μm) in unfaulted protolith decreasing in damage zone cataclasites (10 μm–~900 μm) and – as in the fault centre – increasing to a distribution of (10 μm–1500 μm) in the fault core ultracataclasites (Fig. 8b). At the fault tip maximum pore lengths

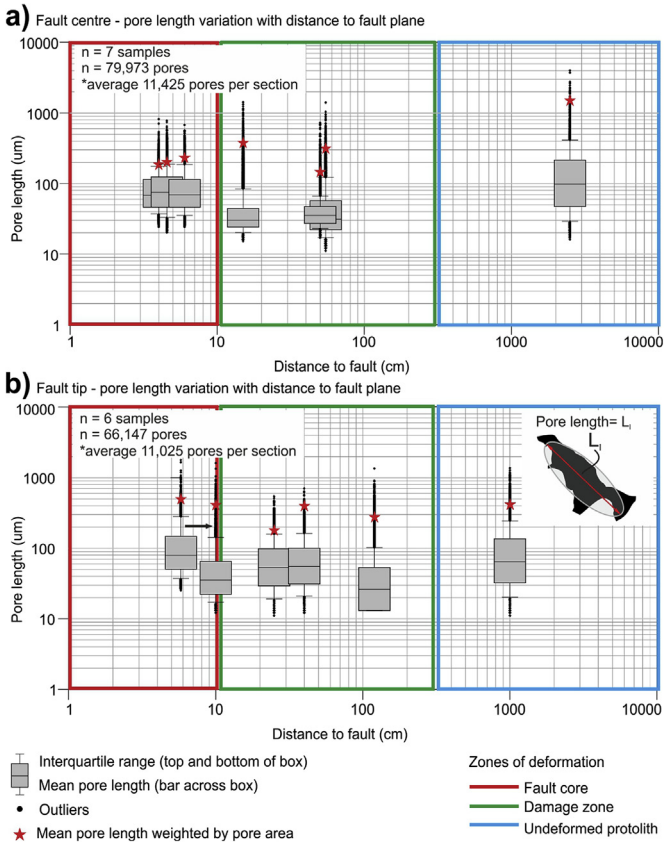

Fig. 8. Graphs showing statistical distributions of pore lengths for (a, b) unfaulted and faulted arenites sampled at varying distances from the Clashach fault. Box and whisker plots show limited change in the interquartile range between samples. Red stars mark the mean value, represented by the pore lengths with the largest contribution to pore area. Arenites from (a) the fault centre locality show an overall decrease in pore length with increased fault deformation while (b) fault tip samples showed some increase in pore length distribution in the fault core. (For interpretation of the references to colour in this figure legend, the reader is referred to the web version of this article.)

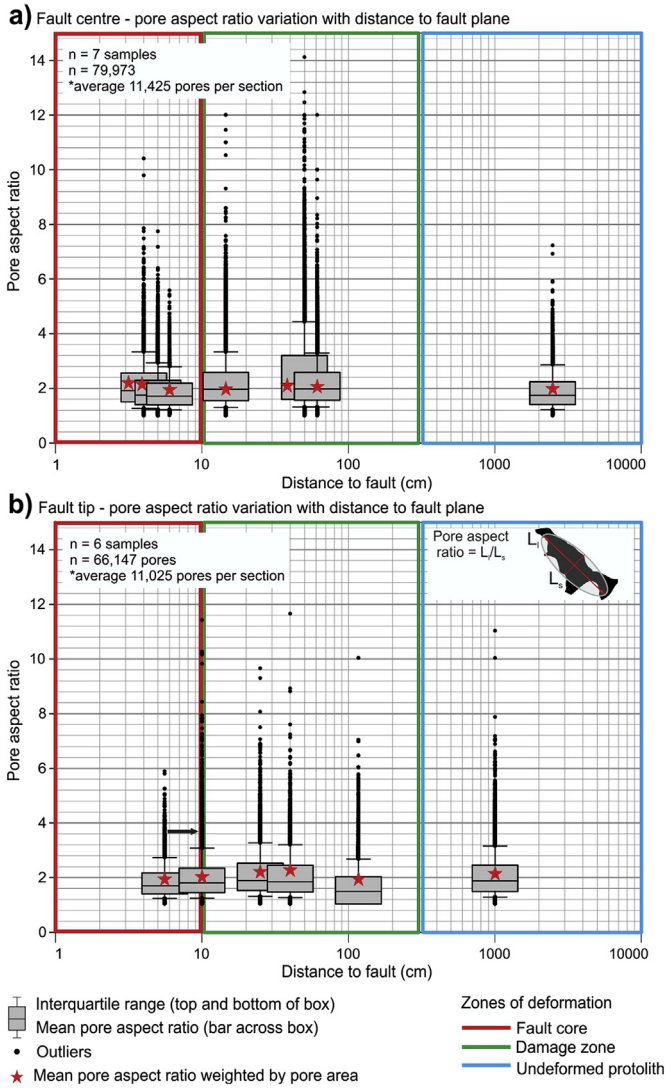

Fig. 9. Graphs showing statistical distributions of pore aspect ratios for unfaulted and faulted arenites sampled at varying distances from the Clashach fault. Arenites from (a) the fault centre locality show an overall decrease in pore aspect ratio with increased fault deformation while (b) fault tip pore showed some increase in pore aspect ratio distribution in the fault core.

were largest in the protolith and fault core (around 1500 μm) and reduced in the damage zone to 500 μm in two samples and around 900 μm in one sample. The mean length of pores - weighted by area – varied a little from a maximum of 500 μm in the fault core down to a minimum of 190 μm in fault damage zone (Fig. 8b).

Pore shape was quantified using pore aspect ratio (Fig. 3d). Results showed that as arenites were faulted and cataclased, the interquartile range of pore aspect ratios - of all samples from both localities - remained similar (>1.2 and < 3.5) (Fig. 9). Fault centre aspect ratio distributions were similar in the protolith and fault core with maximum aspect ratios around 7. Fault centre damage zone aspect ratio distributions were broader with higher maximum aspect ratios around 12 (Fig. 9a). Mean aspect ratio – weighted by area - was about 2 for all samples with a subtle increase from 1.9 to 2.2 in the fault core. Fault tip aspect ratio ranges were similar in unfaulted and faulted samples, however damage zone cataclasites showed slightly higher mean pore aspect ratios compared to the protolith (Fig. 9b).

Pore fabric anisotropy was quantified using the orientation of pore long axes (Fig. 3d). Pore property datasets were filtered by aspect ratio to remove 'sub-isotropic pores' (pores with aspect ratios < 2) that would have less impact on the fabric anisotropy/fluid conductivity. Anisotropic pores make up 10–15% of total number of pores. Pore long axis orientations were quantified and plotted on equal area rose diagrams (Fig. 10). Overall results showed that as arenites were faulted and cataclased, high aspect ratio pores were rotated from sub-horizontal in the unfaulted protolith to sub-vertical in the faulted cataclasites. Orientations measured from unfaulted protolith samples from both the fault tip and fault centre showed anisotropic pores strongly oriented sub-horizontally (Fig. 10a and b). Pores from the fault centre cataclasites remained anisotropic but were reoriented to sub-vertical and at a low angle to the fault dip (Fig. 10a). Pores from some fault core ultracataclasites showed a broad range of orientations therefore making the pore fabric inherently isotropic. Fault tip cataclasites also showed sub-vertical anisotropic pores particularly in the fault damage zone (Fig. 10b).

4.3.2. Arkose

In this section we present the pore geometry attributes for all thin sections as in-situ pores and - for some thin sections - as in-situ pores plus kaolinite filled pores, with perimeters defined by the grains bounding the kaolinite (Fig. 7a). Kaolinite filled pores could only be thresholded by hand therefore only one sample was

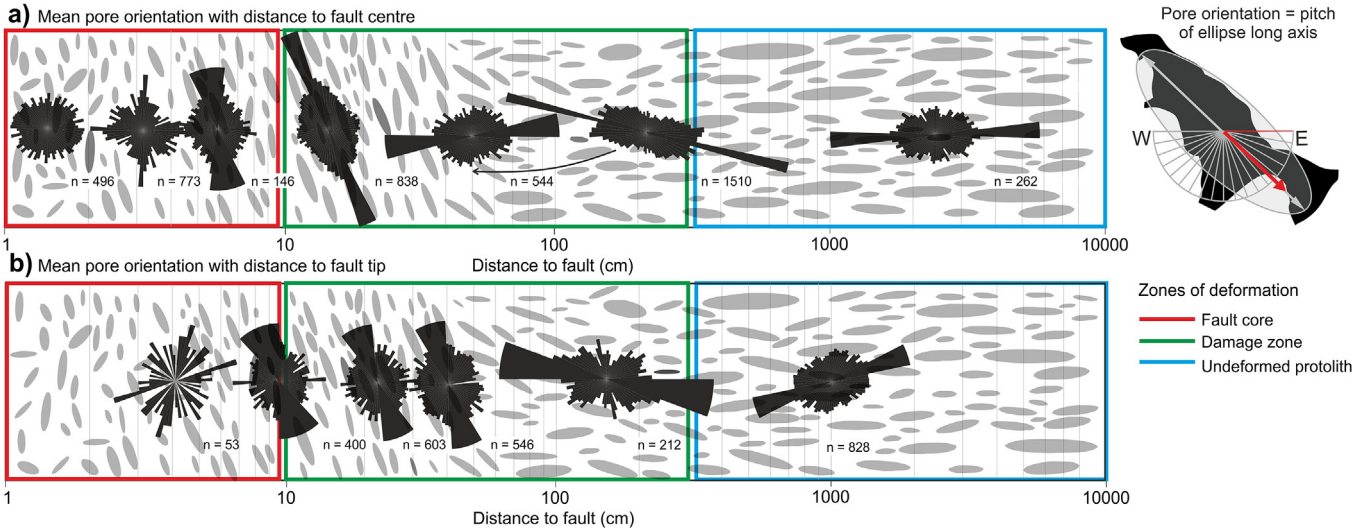

Fig. 10. Plots showing re-orientations of pore long-axis mean orientations from sub-horizontal in unfaulted arenites to sub-vertical in faulted arenites close to the Clashach Fault at both (a) the fault centre and (b) the fault tip. Rose diagrams show the distribution of pore long-axis orientations in each sample and the number of pores sampled.

quantified from each fault architectural zone.

Results showed that as arkoses were intensely fractured and deformed closer to the fault surface, the overall range of pore lengths remained similar to unfaulted protolith distributions (Fig. 11a). A small reduction in the interquartile range of pore lengths was recorded in the least faulted samples (20 and 70 m from the fault surface). Mean pore lengths – weighted by area - were similar in the unfaulted protolith and fault core cataclasites (~150 μm), but were reduced in many damage zone samples (<100 μm) (Fig. 11a). The addition of pores occluded by authigenic kaolinites - to the fabric of in situ pores – made little change to the range of pore lengths but increased maximum pore lengths in all samples particularly faulted arkoses (Fig. 11b). Mean pore lengths increased by 100 μm in protolith and outer damage zone samples. The addition of kaolinite filled pores to inner damage zone and fault core sample pore fabric, increased mean pore length from <100 to 300 μm.

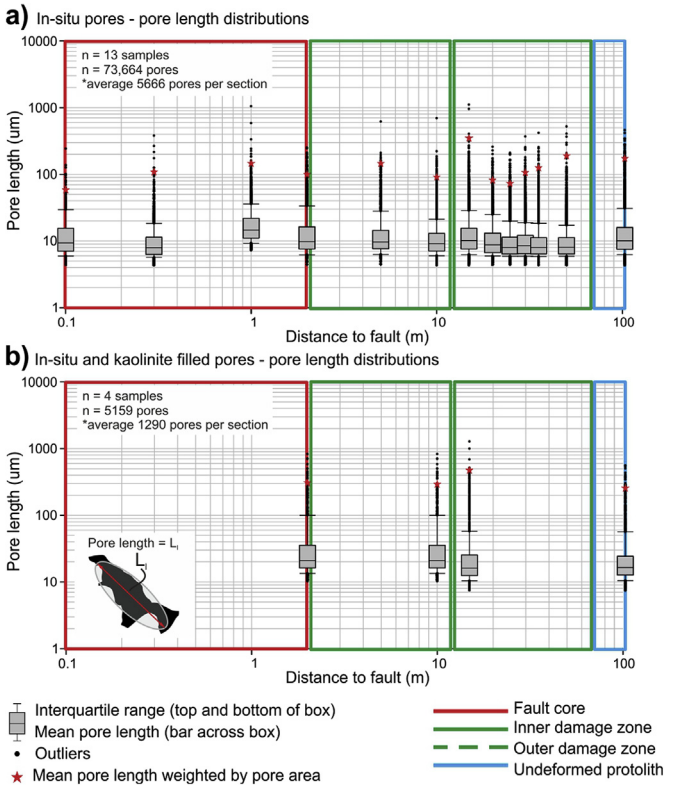

Fig. 11. Graphs showing statistical distributions of pore lengths for unfaulted and faulted arkoses sampled at varying distances to the North Scapa Fault. Lengths have been quantified for (a) in-situ pores and (b) in-situ plus clay filled pores. Box and whisker plots show limited change in the interquartile range between samples. Red stars mark the mean value, represented by the pore lengths with the largest contribution to pore area, this decreases slightly towards the fault plane. (For interpretation of the references to colour in this figure legend, the reader is referred to the web version of this article.)

Results from fractured arkoses in the outer damage zone showed that the aspect ratio ranges of in situ pores remained similar to unfaulted arkoses with interquartile ranges ~ 1.5 to 2.3 in most samples (Fig. 12a). Inner damage zone and fault core samples showed an increase in the range of pore aspect ratios of some samples up to 3.5. Mean pore aspect ratios – weighted by area - were low (1.6–1.7) in the protolith and outer damage zone samples and slightly higher (2.6–4.5) in the inner damage zone and fault core samples (Fig. 12a). Addition of kaolinite filled pores to in situ pore area increased aspect ratio distributions in faulted arkoses, particularly in the fault core (Fig. 12b). Interquartile ranges were increased in most samples to between 1.6 and 3.2 and maximum values increase to 5.2 (Fig. 12b). Mean aspect ratios increased in all faulted samples but remained the same in unfaulted arkose (Fig. 12b).

Pore geometry results showed that as arkoses were faulted and cataclased, the long-axis orientations of in-situ pores - with aspect ratios > 2 - showed no preferred orientations and remained as broadly distributed as orientations quantified from unfaulted arkose pores (Fig. 13a). Inclusion of kaolinite filled pores to the pore fabric decreased the total number of pores (as previously classed in-situ pores were amalgamated). Pore orientations in unfaulted arkoses were distributed bimodally with pores oriented dominantly horizontal and some sub-vertical (Fig. 13b). The inclusion of kaolinite filled pores to damage zone samples also decreased the number of pores (relative to Fig. 13a). In these samples pore orientations were pitching strongly east around 60° (Fig. 13b). Pores from fault core samples were oriented broadly with some bimodal distributions pitching east ~60° and west ~80° (Fig. 13b).

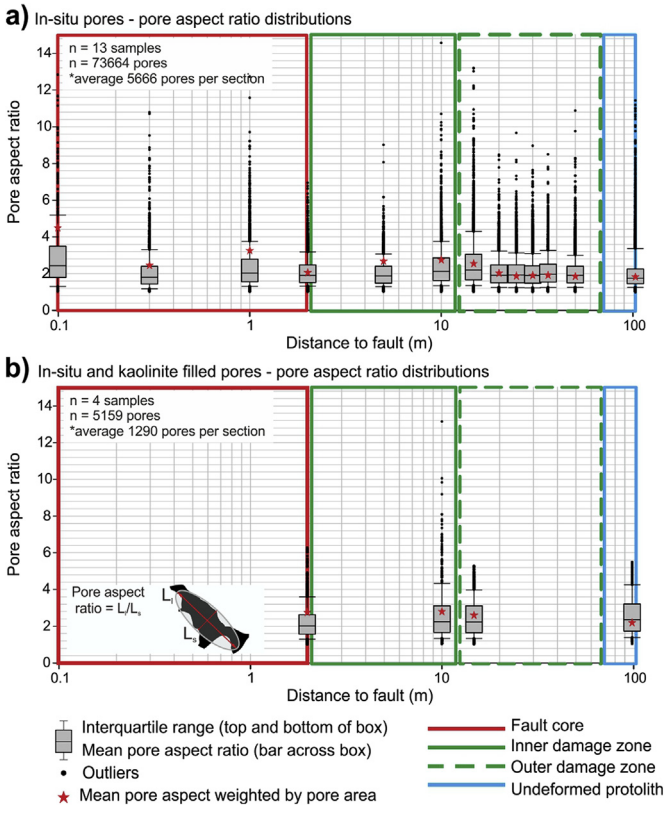

Fig. 12. Graphs showing statistical distributions of pore aspect ratios for unfaulted and faulted arkoses sampled at varying distances to the North Scapa Fault. Aspect ratios quantified for (a) in-situ pores and (b) in-situ plus clay filled pores and showed some increase towards the fault plane.

4.4. Permeability

4.4.1. Arenite permeability

Permeabilities of unfaulted arenite sampled in the footwall, 1000 cm from the Clashach Fault were measured in the framework of core plugs oriented in three orientations to the fault surface (Fig. 3b). Results from 24 core plugs taken from three samples showed maximum permeability in two directions, normal to the fault surface (x) and along fault strike (y). Both x and y core orientations were sub-parallel to sedimentary laminations. Minimum permeabilities were shown in cores oriented parallel to fault dip (z) and sub-perpendicular to sedimentary lamination (Fig. 14a). Twelve faulted arenites sampled from both the hanging wall and footwall - each comprising of a set of three core plugs - also showed anisotropy of permeability in three orientations. The magnitude of anisotropy in each sample varied from less than 1 to more than 3 orders of magnitude (from 0.02 mD to 300 mD) with samples closer to the fault surface tending to show permeabilities ranging over 2 orders of magnitude. The orientation of the anisotropy was also variable, with 6 samples showing maximum permeability (K_{max}) down fault dip (z), 3 samples show K_{max} as along fault strike (y) and 3 samples with K_{max} normal to fault strike (x). Spatial patterns of preferential permeability orientations were evaluated by comparing core plug permeabilities in the two directions with respect to the fault kinematics: along fault strike (y) and parallel to the fault dip direction (z). Maximum permeability is predominantly down fault dip (z) in 9 samples located < 50 cm to the fault surface (highlighted by grey boxes), while 3 samples show K_{max} as along fault strike (y).

4.4.2. Arkose permeability

Results from 9 core plugs of unfaulted arkose showed maximum permeability in two directions, normal to the fault surface (x) and along fault strike (y). Both x and y core orientations were sub-parallel to sedimentary laminations. Permeabilities of core plugs oriented parallel to fault dip (z) and sub-perpendicular to sedimentary lamination were lower but also quite variable (Fig. 15). Fifteen fault rock samples from the Scapa Sandstone Formation, each comprising of a set of three core plugs, also showed anisotropy of permeability in three orientations. The magnitude of anisotropy in each sample varied from less than an order of magnitude to just over 1 order of magnitude. The orientation of the anisotropy was also variable, with 11 samples showing maximum permeability

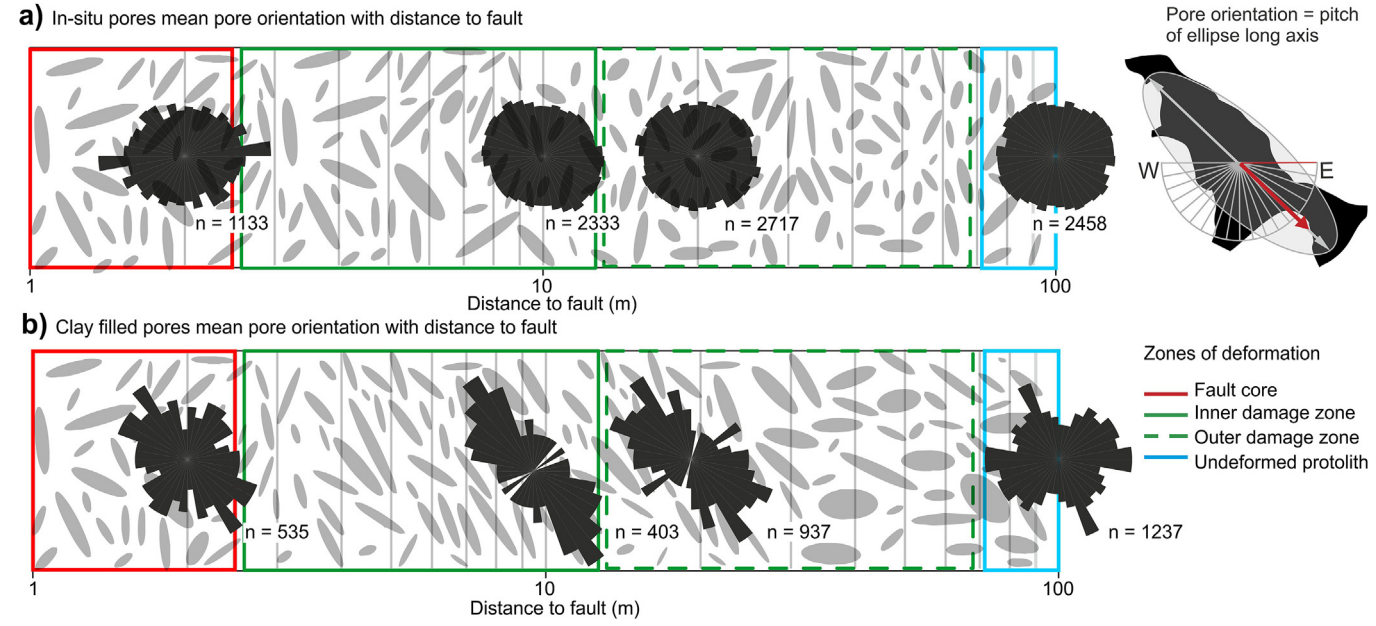

Fig. 13. Plots showing change in the distribution of pore long axis orientations from (a) in-situ pores showing no preferred orientations to (b) a preferred orientation dipping ~60° East with the addition of clay filled pores in faulted arkoses close to the North Scapa Fault. Rose diagrams show the distribution of pore long axis orientations in each sample and the number of pores sampled.

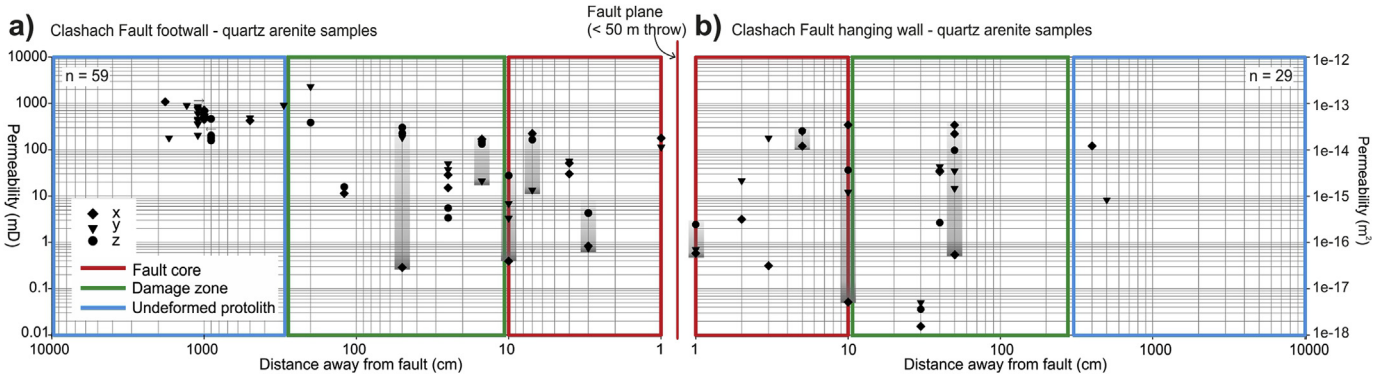

Fig. 14. Graphs showing permeabilities from core plugs collected at a range of distances from the fault plane in the hanging wall and footwall of the Clashach Fault. Eighty eight samples were plugged in three perpendicular orientations with respect to the fault plane, and show anisotropy of permeability within single samples.

(K_{max}) down fault dip (z), 2 samples show K_{max} as along fault strike (y) and 2 samples with K_{max} normal to fault strike (x). In the kinematic directions of a normal fault, down fault dip (z) permeabilities were higher than along fault strike (y) permeabilities in 11 samples (highlighted by grey boxes).

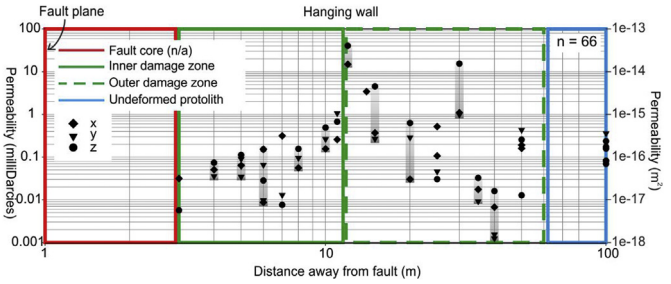

Fig. 15. Graph showing permeabilities from core plugs collected at a range of distances from the fault plane in the hanging wall of the North Scapa Fault. Sixty three samples were core plugged in three perpendicular orientations to the fault plane and show anisotropy of permeability within single samples.

5. Discussion

5.1. Development of arenite pore fabric

Mechanical processes of microfracturing and cataclasis were identified as the main causes of grain size reduction in faulted arenites (Figs. 1 and 6). Grain comminution, which allowed closer packing of grains and restructuring of intergranular pores, was observed as large intergranular pores with complex perimeters in unfaulted arenite became smaller with basic, angular and concave outlines in faulted arenites. This change was quantified in faulted arenites collected at a range of distances from the fault surface as pore lengths reduced with increased deformation from the protolith to the damage zone (Fig. 8). Pores in the fault core showed a non-linear trend as the pore length interquartile range increased relative to the damage zone. This is due to higher intensity of cataclasis and therefore grain reorganisation closer to the fault which destroyed the protolith pore fabrics and allowed development of more stable pore fabrics. Pore aspect ratios were moderately anisotropic in both unfaulted and faulted arenites with few larger aspect ratio pores in fault core samples from the centre of the fault (Fig. 9). However the long-axis orientation of these anisotropic pores changed substantially from sub-horizontal in the unfaulted samples to sub-vertical in faulted samples (Fig. 10). Development of anisotropic pores oriented sub-vertically - or in the context of the normal fault, at a low angle to the maximum principal stress (σ_1) - in faulted arenites can be visualised through the void cell model (Li and Li, 2009). In this model, anisotropic pore structures with long axes oriented perpendicular (or at a high angle) to the maximum principal stress (as identified in unfaulted arenites) are weak and will collapse under increasing differential stress, leaving the more stable elongate pores (oriented at lower angles to σ_1) open, thereby available to dominate the bulk porosity in faulted arenites (Farrell et al., 2014). This scheme for porosity evolution has been applied to DEM modelling for unconsolidated materials (Kang et al., 2012), but could also apply in consolidated granular rocks where cemented grains are quasi-continually broken apart by cataclasis, the dominant deformation mechanism identified in most studies of faulted porous sandstones (e.g. Saillet and Wibberley, 2010; Fossen et al., 2007; Aydin and Johnson, 1978). The mechanics and kinematics of grain-scale cataclasis involves an initial dilatancy to allow for grain breaking, including some shearing, followed by reorganisation of grains and subsequent compaction (Antonellini and Aydin, 1994). Episodes of dilatancy in developing fault rocks could allow for the development of new pore space, which is only preserved if oriented sub-vertically so that it is stable against the maximum principal stress (30° from the down fault dip direction in a normal fault). In comparison compaction and destruction of unfavourably oriented pores would occur perpendicular to the maximum principal stress.

Chemical processes of quartz cement precipitation around quartz grains and infilling intergranular fractures has also reduced intergranular and microfracture porosity in faulted arenites (Fig. 16a and c). Quantification of quartz cements from SEM-CL (Scanning Electron Microscope Cathodoluminescence) images have shown increased cement content with increased proximity to the fault surface. Quartz cement was present in all damage zone samples but was absent in some ultracataclasites in the fault core as they were occluded with silica-rich gouge (Fig. 16d). This indicates that cements were precipitated after ultracataclasis reduced grains to silica-rich gouges. Quartz overgrowths precipitate preferentially onto 'fresh' grain boundaries formed during grain comminution. In the faulted arenites, 'fresh' grain boundaries often comprise fracture surfaces which form with their long-axis parallel to the principal maximum stress. Quartz overgrowths grow perpendicular to the grain boundaries. In the faulted arenites this would narrow the short-axis of fault-induced pores and increase the aspect ratio of pores oriented at a low angle to σ_1 (Fig. 9). Preferred precipitation of quartz onto microfracture surfaces that are free from clay and iron oxide coats is also identified in a previous study on faulted quartz arenites (Eichhubl et al, 2010). Authigenic quartz cements identified in faulted arenites were highly luminescent in

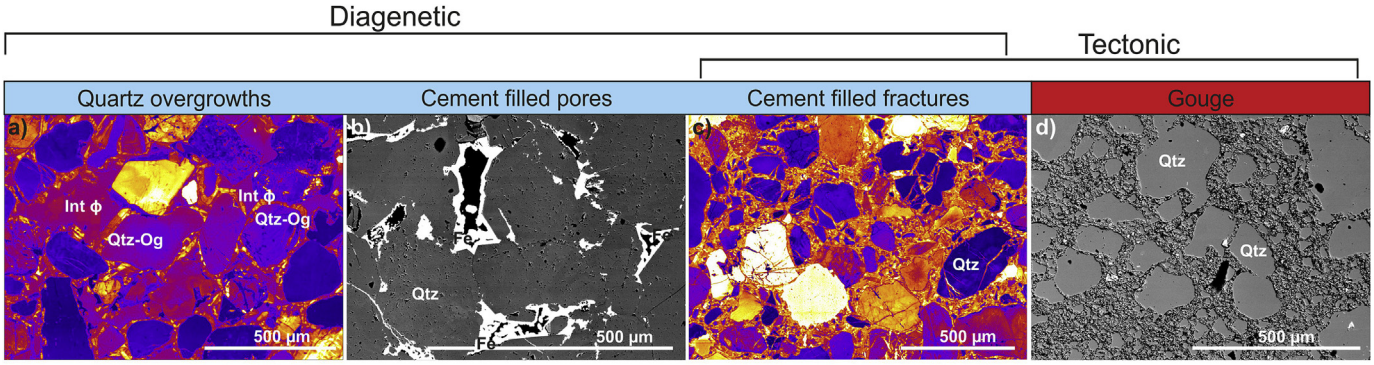

Fig. 16. (a, c) SEM-BSE and (b, d) SEM-CL images of faulted quartz-rich arenite showing (a) euhedral quartz cement overgrowths (Qtz-Og) and (b) iron cement (Fe) occluding intergranular pores (Int ϕ). (c) Highly luminescent, fault related quartz cements occluding tectonic microfractures and grains which have been broken up via cataclasis. (d) Ultra-cataclased quartz grains occlude all porosity in highly deformed fault core samples forming the matrix surrounding rounded survivor grains.

comparison to detrital quartz grains. Fracture filling quartz cement and overgrowths were variably luminescent showing a jaggedy, mottled texture (Fig. 16c). These textures have not been documented in previous studies but could be created by precipitation during faulting as they appeared to show rapid formation rather than multiple phases of cementation which would create classically euhedral overgrowths with banding reflecting minor variations in fluid chemistry over time (Walker and Burley, 1991). Quantification of quartz cements around the Clashach fault will be further addressed in a future study.

5.2. Development of arkose pore fabric

Fracturing (tensile and shear), cataclasis and brecciation were the main mechanical deformation mechanisms inferred in samples of faulted arkose (Figs. 2 and 7). Macro and micro fractures identified in the 'outer damage zone' samples enhanced the original host rock porosity forming a rock with similar pore fabric as the unfaulted sample plus more higher aspect ratio pores (Fig. 5). Macro fractures visible in hand samples and core plugs were under sampled in thin sections, therefore pore lengths and aspect ratios are probably higher in nature than recorded. Cataclasis and microfracturing were identified as the main causes of grain size reduction in arkoses from the 'inner damage zone' and fault core (Fig. 2). In these samples although grain comminution allowed closer packing of grains, the intergranular pore fabric was shown to have comparable pore size distribution in unfaulted samples (Fig. 11) with slightly broader pore aspect ratio distributions (Fig. 12). Grains were not rotated and reorganised during cataclasis in faulted arkoses as they are in arenites (Section 5.1) because the original grain packing in the unfaulted arkose was too tight with long grain contacts that would not allow enough dilation for grain rotation, therefore intergranular pores showed no preferred long axis orientations.

Secondary pores formed by the chemical process of feldspar dissolution were common in both unfaulted and faulted samples (Fig. 7). The amount of secondary porosity was variable between samples accounting for over 50% of total porosity in the outer damage zone and protolith (Fig. 7e). In the unfaulted samples, secondary pore shape was generally rounded with a low aspect ratio, reflecting the shape of unfaulted feldspar grains. In contrast cataclased fault samples contained highly deformed K-feldspar grains that had been broken up and sheared, changing the grain boundaries from coherent, low aspect ratio, blocky grains in unfaulted samples to strung out, elongate grains in faulted samples. Fault deformed K-feldspars tended to be oriented parallel to the fault slip plane due to the direction of shearing. The shapes of these faulted grains were considered to control the shapes of secondary pores produced by grain dissolution.

5.3. Faulted sandstone pore fabrics and permeability

From previous studies of faulted sandstone porosity we know that mineralogy, grain size, the amount and nature of grain contacts, pre-existing pore network and diagenetic history of the protolith all exert some control on the development of post-faulting microstructure, and therefore pore fabric (Pittman, 1981; Aydin and Johnson, 1978; Blenkinsop, 1991; Antonellini et al., 1994; Fowles and Burley, 1994; Johansen et al., 2005; Torabi and Fossen, 2009; Menendez et al., 1996). In addition, we can add: fault displacement, fault kinematics, deformation mechanisms and depth of faulting. Although previous studies have identified the effects of these fault-related variables on the amount of porosity, no previous studies have quantified these changes in terms of the variations in specific pore attributes with fault deformation. This has the consequence that porosity data from previous studies cannot be as comprehensively linked to other laboratory derived rock properties, such as permeability or strength.

Results from this study show that permeability decreases with increasing deformation closer to the fault surface (Figs. 14 and 15). These results concur with permeability studies on naturally deformed porous sandstone (Chester and Logan, 1986; Antonellini and Aydin, 1994) and laboratory deformed rocks (Zhu and Wong, 1997). Further to this, faulted samples exhibit preferential permeability pathways parallel to fault dip in both arenites and arkoses. Pore fabric results from both arenites and arkoses show that in sandstones which have been deformed closer to the fault, pore fabrics are anisotropic with intergranular pores and/or secondary dissolution pores oriented sub-parallel to the fault dip. Anisotropy of permeability is most pronounced in faulted arenites, showing permeabilities of variably oriented core plugs from a single sample ranging up to 3 orders magnitude. While the degree of anisotropy of permeability in faulted arkoses is lower – usually less than 1 order of magnitude. Dissolution of detrital K-feldspar grains tends to form large pores with limited connectivity in unfaulted arkoses, however results indicate that the pore occluding kaolinite (replacing the K-feldspar) does not inhibit fluid flow pathways unlike pore lining clays such as illite and chlorite (Neasham, 1977). It should be noted that permeability tests in this study were run with N_2 gas as a pore fluid – in a sub-surface environment the presence of hydrous liquid phases could cause volume changes in the kaolinites within these pores which could limit permeability and/or produce other anisotropic effects (Faulkner and Rutter, 2000; Tanikawa and Shimamoto, 2009). A limitation of using core

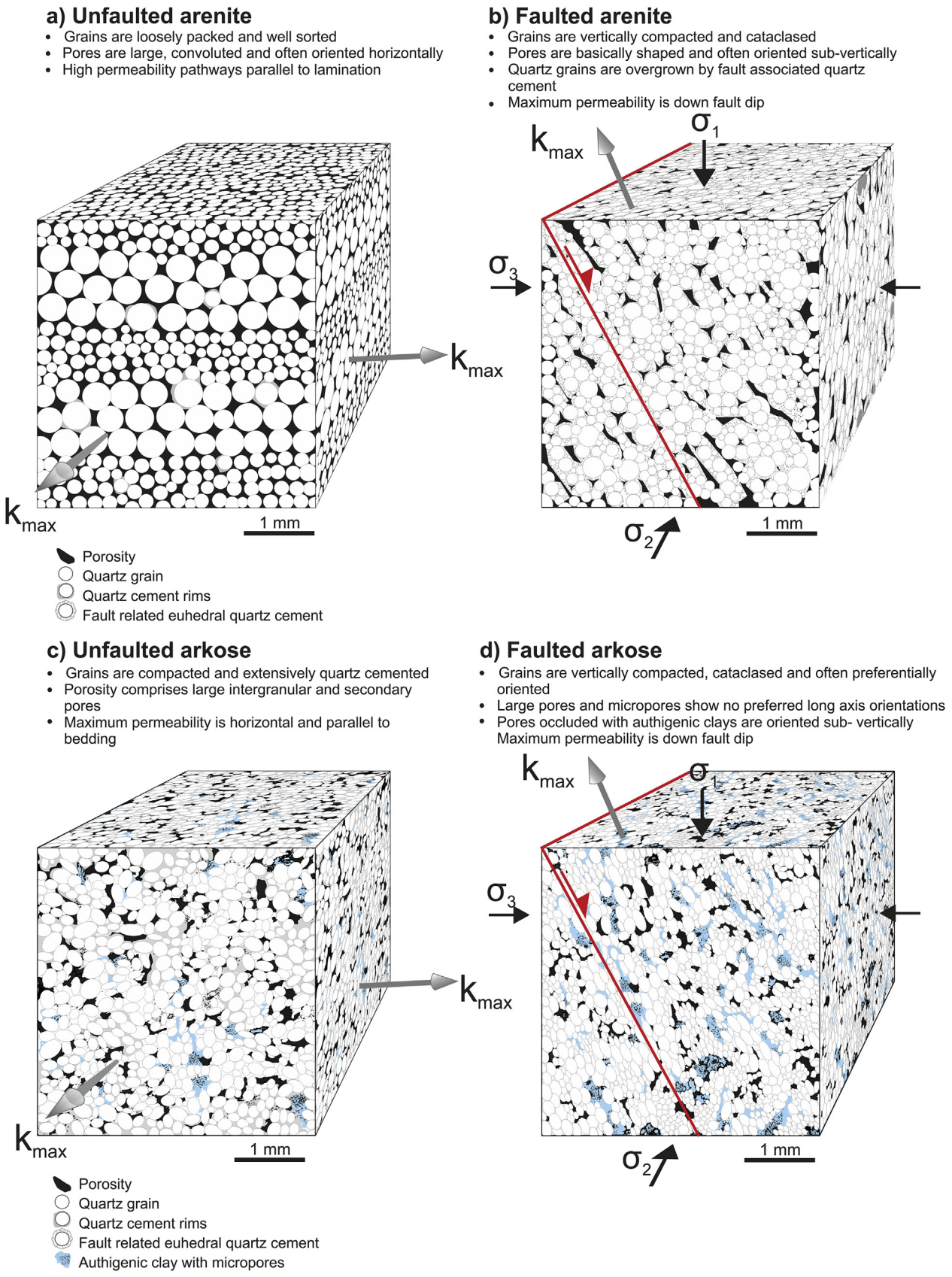

Fig. 17. Schematic block diagrams showing how porosities and permeabilities evolve with deformation in (a, b) an arenite protolith and (c, d) an arkose protolith.

plugs to measure permeability is that the sample sizes are too small to include some macroscopic features. Macro–structural field data was also collected around i.e. fracture intensity, lengths, apertures, orientations. To better relate this data to reservoir fault models, the estimated permeabilities of these features could be incorporated with core plug permeabilities.

Processes controlling *grain* fabric modification are dominated by fracturing and cataclasis in both sandstones. However the processes controlling the resultant *pore* fabric vary between the two sandstones with pore modification in the arenites dominated by chemical processes of preferential cement precipitation while dissolution of increasingly deformed K-feldspars control the modified pore fabric in the arkose. Previous work on faulted sandstones recognises both mechanical processes of fracturing and cataclasis (e.g. Anders and Wiltschko, 1994; Saillet and Wibberley, 2010; Fossen et al., 2007; Aydin and Johnson, 1978) and chemical processes of quartz cementation and grain dissolution (Bernabe et al., 1992; Reed and Laubach, 1996). Therefore pore fabrics identified in this study are likely to be quantifiable around other sandstone hosted faults.

5.4. Using quantified pore fabrics in geomechanical models

Previous experimental research on porous sandstones has shown that during increases in pore fluid pressure, higher porosity can reduce the compressive strength of a rock and reduce the effective normal stress leading to fault reactivation (Scott and Neilson, 1991). However no studies on experimentally or naturally faulted sedimentary rocks have incorporated the pore attributes of aspect ratio and long-axis orientations in geomechanical models. Our study has shown that high porosities in the unfaulted protolith tended to decrease with faulting. Mean pore aspect ratios quantified from unfaulted and faulted rocks were moderate around 2. However the geometry of pores was changed by faulting and pores were reoriented from sub-horizontal and normal to σ_1 in the unfaulted rocks, to sub-parallel to σ_1 in the faulted rocks. Theoretical studies modelling the poroelastic effects of increasing pore fluid pressure in rocks with anisotropic pores oriented parallel to σ_1 show that, as well as decreasing the effective normal stress, the shear stress is increased (Chen and Nur, 1992; Healy, 2012; Farrell, 2016; *unpublished PhD thesis*). Therefore pores in the faulted arenite may contribute to this anisotropic poroelastic response, and increase the geomechanical risk of fault slip during increases in pore fluid pressure.

6. Summary

Petrophysical and geometrical analyses have been conducted to examine the relationship between porosity and pore fabrics to fluid flow and permeability anisotropy, on samples collected from two normal fault zone outcrops hosted in a 'clean' quartz-rich arenite and a 'muddy' quartz sub-arkose. Differences between the unfaulted microstructure of these porous sandstones are illustrated on block diagrams (Fig. 17a and c). These models show that originally the grain structure of unfaulted arenite was well-sorted, loosely packed and fine to medium grained while unfaulted arkoses were well-sorted, closely packed and fine grained with extensive quartz cements overgrowing groups of grains. The K-feldspar content of unfaulted arenites comprised an average 7% while unfaulted arkoses comprised an average 14% K-feldspar. The porosity of unfaulted arenites was up to 27% while unfaulted arkoses had up to 13% porosity.

From microstructural studies the mechanisms of deformation in sandstones can be classified broadly into two types. Cataclastic deformation, where the mineralogy is not changed but the microstructural arrangement is altered by fracturing and comminution of grains and shearing and sliding of grain fragments. Chemical deformation, where grain shape is changed by pressure solution as grains are dissolved and reprecipitated. Analysis of mechanical and post-faulting chemical deformation mechanisms around the two faults concluded that cataclasis and grain comminution occurred at a greater extent closer to both fault surfaces. In high porosity arenites the results of cataclasis were reorganisation of grains and generation of a new - mechanically generated - intergranular pore fabric. In the lower porosity arkoses the results of cataclasis were crushing and shearing of weaker K-feldspar grains which were later dissolved leaving new - chemically generated - secondary dissolution pore fabrics often filled with authigenic kaolinite.

The consequences of faulting being dominated by different deformation mechanisms in the arenite versus the arkose for fault rock pore fabrics were that: normal faulting of arenites produced fault-deformed rocks with evenly distributed, anisotropic pores oriented at a low angle to σ_1 (Fig. 17b) while normal faulting of arkoses generated rocks with bimodal pore sizes and irregular pore distributions as well as highly anisotropic kaolinite-filled pores oriented sub-parallel to the fault surface (Fig. 17d).

General conclusions about the relationships between pore properties and fault zone architecture have been made from this pore fabric quantification including.

1. Sandstones closer to the fault surface are more likely to have decreased porosities, i.e. less than half the porosity of unfaulted protolith.
2. Closer to the fault surface the pore fabrics of faulted sandstones are more anisotropic.
3. Closer to the fault surface pore orientations are more likely to reflect the fault surface orientation close to the orientation of the maximum principal stress (σ_1).

Core plug measurements from this study show anisotropy of permeability in sandstone hosted normal faults. Quantitative study of complex pore geometries from samples collected along the fault zone have shown that the main impacts of faulted sandstone pore fabrics on permeability were.

1. Lower porosities close to the fault surface *reduces* bulk permeability, though this can *enhance* the magnitude of any permeability *anisotropies.*
2. Anisotropic pores induce anisotropy of permeability in faulted rocks. This can also change any inherent permeability anisotropies present in the unfaulted protolith (Fig. 17a and c).
3. Anisotropic pores close to the fault surface form high permeability pathways oriented parallel to fault dip (Fig. 17b and d).

Quantitative pore characterisation in this study has made it possible to attribute changes in porosity and pore fabric to processes of mechanical and chemical deformation and quantification of these pores can be used to understand anisotropy of fluid flow around fault zones. By quantifying these microstructural properties in a spatial framework around the fault and in the context of the sandstone facies, our results can be used to infer pore fabric patterns around other sandstone-hosted normal faults. Advances in data acquisition from hardware such as X-ray CT and synchrotron sources, coupled with on-going refinements to software tools such as ImageJ, present us with new opportunities to quantify the pore space in rocks. We are no longer restricted to scalar values of porosity as isolated bulk measurements. We can accurately measure pore shapes, sizes and orientations, and more importantly, the statistical and spatial variations of these attributes to create

quantified pore fabrics of faulted rocks. The challenge now is to systematically collect more of these datasets and then to improve our understanding of how they relate to the transport and mechanical properties of faulted and fractured rock.

Acknowledgements

Thanks to SEM technician Peter Chung at the University of Glasgow, David Wilde and Peter Greatbatch at Keele University for careful thin section preparation, Chris Wibberley and Tom Blenkinsop for input and Kieran Keith from Harlaw Academy, Aberdeen for help collecting petrophysical data. Thanks to Fabrizio Storti, Michael Heap and Toru Takeshita for helping to improve this paper with their constructive reviews. This work forms part of a NERC Standard award for DH (NE/N003063/1), which is gratefully acknowledged.

References

Al-Gharbi, M.S., Blunt, M.J., 2005. Dynamic network modeling of two-phase drainage in porous media. Phys. Rev. E 71 (1), 016308.
Anders, M.H., Wiltschko, D.V., 1994. Microfracturing, palaeostress and the growth of faults. J. Struct. Geol. 16, 795–815.
Anselmetti, F.S., Luthi, S., Eberli, G.P., 1998. Quantitative characterisation of carbonate pore systems by digital image analysis. AAPG Bull. 82–10, 1815–1836.
Antonellini, M., Aydin, A., 1994. Effects of faulting on fluid flow in porous sandstone: petrophysical properties. AAPG Bull. 78, 355–377.
Antonellini, M., Aydin, A., Pollard, D.D., d'Onfro, P., 1994. Petrophysical study of faults in sandstone using petrographic image analysis and x-ray computerized tomography. Pure Appl. Geophys. 143 (1–3), 181–201.
Aydin, A., Johnson, A.M., 1978. Development of faults as zones of deformation bands and slip surfaces in sandstone. Pure Appl. Geophys. 116, 931–942.
Bakke, S., Øren, P.E., 1997. 3-D pore-scale modelling of sandstones and flow simulations in the pore networks. Spe J. 2 (02), 136–149.
Balsamo, F., Storti, F., Salvini, F., Silva, A.T., Lima, C.C., 2009. Structural and petrophysical evolution of extensional fault zones in low-porosity, poorly lithified sandstones of the Barreiras Formation, NE Brazil. J. Struct. Geol. 32, 1806–1826.
Baud, P., Klein, E., Wong, T.F., 2004. Compaction localization in porous sandstones: spatial evolution of damage and acoustic emission activity. J. Struct. Geol. 26 (4), 603–624.
Benson, P.M., Meredith, P.G., Platzman, E.S., 2003. Relating pore fabric geometry to acoustic and permeability anisotropy in Crab Orchard Sandstone: a laboratory study using magnetic ferrofluid. Geophys. Res. Lett. *30* (19).
Bernabe, Y., Fryer, D.T., Hayes, J.A., 1992. The effect of cement on the strength of granular rocks. Geophys. Res. Lett. 19, 1511–1514.
Biegel, R.L., Sammis, C.G., Dieterich, J.H., 1989. The frictional properties of a simulated gouge having a fractal particle distribution. J. Struct. Geol. 11 (7), 827–846.
Blair, S.C., Berge, P.A., Berryman, J.G., 1996. Using two-point correlation functions to characterize microgeometry and estimate permeabilities of sandstones and porous glass. J. Geophys. Res. 101, 20,359–20,375.
Blenkinsop, T.G., 1991. Cataclasis and process of particle size reduction. Pure Appl. Geophys. 136, 59–86.
Blunt, M.J., 2001. Flow in porous media—pore-network models and multiphase flow. Curr. Opin. colloid & interface Sci. 6 (3), 197–207.
Bryntesson, L., Mattias, 2002. Pore network modelling of the behaviour of a solute in chromatography media: transient and steady-state diffusion properties. J. Chromatogr. A 945 (1), 103–115.
Bubeck, A., Walker, R.J., Healy, D., Dobbs, M., Holwell, D.A., 2017. Pore geometry as a control on rock strength. Earth Planet. Sci. Lett. 457, 38–48.
Byerlee, J.D., 1967. Frictional characteristics of granite under high confining pressure. J. Geophys. Res. 72 (14), 3639–3648.
Byerlee, J., Summers, R., 1976. A note on the effect of fault gouge thickness on fault stability. In: International Journal of Rock Mechanics and Mining Sciences & Geomechanics Abstracts, vol. 13. Pergamon, pp. 35–36, 1.
Caine, J.S., Evans, J.P., Forster, C.B., 1996. Fault zone architecture and permeability structure. Geology 24, 1025–1028.
Carroll, 1979. An effective stress law for anisotropic elastic deformation. J. Geophys. Res. 84, 7510.
Chen, Q., Nur, A., 1992. Pore fluid pressure effects in anisotropic rocks: mechanisms of induced seismicity and weak faults. PAGEOPH 139.
Chester, F.M., Logan, J.M., 1986. Implications for mechanical properties of brittle faults from observations of the Punchbowl fault zone, California. Pure Appl. Geophys. 124 (1–2), 79–106.
Colombier, M., Wadsworth, F.B., Gurioli, L., Scheu, B., Kueppers, U., Di Muro, A., Dingwell, D.B., 2017. The evolution of pore connectivity in volcanic rocks. Earth Planet. Sci. Lett. 462, 99–109.
David, C., Wong, T., Zhu, W., Zhang, J., 1994. Laboratory measurements of compaction induced permeability change in porous rocks: implications for the generation and maintenance of pore pressure excess in the crust. PAGEOPH 142.
Davis, T., Healy, D., Bubeck, A., Walker, R.J., 2017. Stress concentrations around voids in three dimensions: the roots of failure. J. Struct. Geol. 102, 193–207.
Dieterich, J.H., 1981. Constitutive properties of faults with simulated gouge. Mech. Behav. Crustal Rocks Handin. Vol. 103–120.
Dunn, D.E., LaFountain, L.J., Jackson, R.E., 1973. Porosity dependence and mechanism of brittle fracture in sandstones. J. Geophys. Res. 78 (14), 2403–2417.
Ehrlich, R., Kennedy, S.K., Crabtree, S.J., Cannon, R.L., 1984. Petrographic image analysis: I. Analysis of reservoir pore complexes. J. Sediment. Petrol. 54, 1515–1522.
Eichhubl, P., Hooker, J.N., Laubach, S.E., 2010. Pure and shear-enhanced compaction bands in Aztec Sandstone. J. Struct. Geol. 32, 1873–1886.
Engelder, J.T., 1974. Cataclasis and the generation of fault gouge. Geol. Soc. Am. Bull. 85–10, 1515–1522.
Etris, E.L., Brumfield, D.S., Ehrlich, R., 1988. Relations between pores, throats and permeability: a petrographic/physical analysis of some carbonate grainstones and packstones. Carbonates Evaporites 3–1, 17–32.
Faulkner, D.R., Rutter, E.H., 2000. Comparisons of water and argon permeability in natural clay-bearing fault gouge under high pressure at 20° C. J. Geophys. Res. Solid Earth 105 (B7), 16415–16426.
Farquharson, J., Heap, M.J., Varley, N.R., Baud, P., Reuschlé, T., 2015. Permeability and porosity relationships of edifice-forming andesites: a combined field and laboratory study. J. Volcanol. Geotherm. Res. 297, 52–68.
Farrell, N.J.C., Healy, D., Taylor, C.W., 2014. Anisotropy of permeability in faulted porous sandstones. J. Struct. Geol. 63, 50–67.
Farrell, N.J.C., 2016. Quantifying Fault Stability. Unpublished PhD thesis. University of Aberdeen.
Fisher, Q.J., Casey, M., Clennell, B., Knipe, R.J., 1999. Mechanical compaction of deeply buried sandstones of the North Sea. Mar. Petrol. Geol. 16, 605–618.
Fossen, H., Schultz, R.A., Shipton, Z.K., Mair, K., 2007. Deformation bands in sandstone: a review. J. Geol. Soc. Lond. 164, 755–769.
Fowles, J., Burley, S., 1994. Textural and permeability characteristics of faulted, high porosity sandstones. Mar. Petrol. Geol. 11, 608–623.
Glennie, K.W., Mudd, G.C., Nagtegaal, P.J.C., 1978. Depositional environment and diagenesis of permian rotliegendes sandstones in leman bank and sole pit areas of the UK southern North Sea. J. Geol. Soc. 135 (1), 25–34.
Grattoni, C.A., Dawe, R.A., 1994. Pore structure influence on the electrical resistivity of saturated porous media. In: SPE Latin America/Caribbean Petroleum Engineering Conference. Society of Petroleum Engineers.
Griffiths, L., Heap, M.J., Xu, T., Chen, C.F., Baud, P., 2017. The influence of pore geometry and orientation on the strength and stiffness of porous rock. J. Struct. Geol. 96, 149–160.
Gueguen, Y., Dienes, J., 1989. Transport properties of rocks from statistics and percolation. Math. Geol. 21 (1), 1–13.
Healy, D., 2012. Anisotropic Poroelasticity and the Response of Faulted Rock to Changes in Pore-fluid Pressure, vol. 367. Geological Society of London, Special Publications, pp. 201–214.
Hillis, R.R., 2001. Coupled changes in pore pressure and stress in oil fields and sedimentary basins. Pet. Geosci. 7 (4), 419–425.
Hippler, S.J., 1993. Deformation microstructures and diagenesis in sandstone adjacent to an extensional fault: implications for the flow and entrapment of hydrocarbons. AAPG Bull. 77 (4), 625–637.
Johansen, T.E.S., Fossen, H., Kluge, R., 2005. The impact of syn-faulting porosity reduction on damage zone architecture in porous sandstone: an outcrop example from the Moab Fault, Utah. J. Struct. Geol. 27, 1469–1485.
Kang, D.H., Yun, T.S., Lau, Y.M., Wang, Y.H., 2012. DEM simulation on soil creep and associated evolution of pore characteristics. Comput. Geotech. 39, 98–106.
Keehm, Y., Mukerji, Nur, A., 2001. Computational rock physics at the pore scale: transport properties and diagenesis in realistic pore geometries. Lead. Edge 20 (2).
Klinkenberg, L.J., 1941. The permeability of porous media to liquids and gases. In: Am Pet Inst Drill Prod Pract, pp. 200–213.
Kuster, G.T., Toksöz, M.N., 1974. Velocity and attenuation of seismic waves in two-phase media: Part II. Experimental results. Geophysics 39 (5), 607–618.
Lander, R.H., Larese, R.E., Bonnell, L.M., 2008. Towards more accurate quartz cement models: the importance of euhedral versus noneuhedral growth rates. AAPG Bull. 92, 1537–1563.
Li, X., Li, X., 2009. Micro-macro quantification of the internal structure of granular materials. J. Eng. Mech. 135–7, 641–656.
Lindquist, S.J., 1988. Practical characterisation of eolian reservoirs for development: nugget Sandstone, Utah-Wyoming thrust belt. In: Kocurek, G. (Ed.), Late Paleozoic and Mesozoic Eolian Deposits of the Western Interior of the United States. Sedimentary Geology, vol. 56, pp. 315–339.
Louis, L., David, C., Robion, P., 2003. Comparison of the anisotropic behaviour of undeformed sandstones under dry and saturated conditions. Tectonophysics 370 (1), 193–212.
Lucia, F.J., 1995. Rock-fabric/petrophysical classification of carbonate pore space for reservoir characterization. AAPG Bull. 79 (9), 1275–1300.
Manzocchi, T., Ringrose, P.S., Underhill, J.R., 1998. Flow through fault systems in high-porosity sandstones. In: Coward, M.P., Daltaban, T.S., Johnson, H. (Eds.), Structural Geology in Reservoir Characterization. Geological Society, vol. 127. Special Publications, London, pp. 65–82.
Marone, C., Scholz, C.H., 1989. Particle-size distribution and microstructures within simulated fault gouge. J. Struct. Geol. 11 (7), 799–814.
McBride, E.F., 1989. Quartz cement in sandstones: a review. Earth Sci. Rev. 26, 69–112.

McBride, E.F., Milliken, K.L., Cavazza, W., Cibin, U., Fontana, D., Picard, M.D., Zuffa, G.G., 1995. Heterogeneous distribution of calcite cement at the outcrop scale in Tertiary sandstones, northern Apennines, Italy. AAPG Bull. 79 (7), 1044–1062.
Mees, F., Swennen, R., Van Geet, M., Jacobs, P., 2003. Applications of X-ray Computed Tomography in the Geosciences. Geological Society, vol. 215. Special Publications, London, pp. 1–6 (1).
Menendez, B., Zhu, W., Wong, T.F., 1996. Micromechanics of brittle faulting and cataclastic flow in Berea sandstone. J. Struct. Geol. 18, 1–16.
Neasham, J.W., 1977. The morphology of dispersed kaolinite in sandstone reservoirs and its effect on sandstone shaliness, pore space and fluid flow properties. In: SPE Annual Fall Technical Conference and Exhibition. Society of Petroleum Engineers.
Oda, M., Nemat-Nasser, S., Konishi, J., 1985. Stress-induced anisotropy in granular masses. Soils Found. 25–3, 85–97.
Oda, M., 1982. Fabric tensor for discontinuous geological materials. Soil Found. 22 (4), 96.
Okabe, H., Blunt, M.J., 2004. Prediction of permeability for porous media reconstructed using multiple-point statistics. Phys. Rev. E 70 (6), 066135.
Paxton, S.T., Szabo, J.O., Ajdukiewicz, J.M., Klimentidis, R.E., 2002. Construction of an intergranular volume compaction curve for evaluating and predicting compaction and porosity loss in rigid-grain sandstone reservoirs. AAPG Bull. 86–12, 2047–2067.
Pittman, E.D., 1981. Effect of fault-related granulation on porosity and permeability of quartz sandstones, Simpson Group (Ordovician) Oklahoma. AAPG Bull. 65, 2381–2387.
Pittman, E.D., 1992. Relationship of porosity and permeability to various parameters derived from mercury injection-capillary pressure curves for sandstone (1). AAPG Bull. 76 (2), 191–198.
Raymer, L.L., Hunt, E.R., Gardner, J.S., 1980. An improved sonic transit time-to-porosity transform. In: Trans. SPWLA 21st Annu. Log. Symp, pp. P1–P13.
Reed, R.M., Laubach, S.E., 1996. The role of microfractures in the development of quartz overgrowth cements in sandstones: new evidence from cathodoluminescence studies (abs.). Geol. Soc. Am. Abstr. Prog. 28–7, A280.
Robion, P., David, C., Dautriat, J., Colombier, J.C., Zinsmeister, L., Collin, P.Y., 2014. Pore fabric geometry inferred from magnetic and acoustic anisotropies in rocks with various mineralogy, permeability and porosity. Tectonophysics 629, 109–122.
Ruzyla, K., 1986. Characterization of pore space by quantitative image analysis. SPE Form. Eval. 1 (04), 389–398.
Saar, M.O., Manga, M., 1999. Permeability-porosity relationship in vesicular basalts. Geophys. Res. Lett. 26, 111–114.
Saillet, E., Wibberley, C.A.J., 2010. Evolution of cataclastic faulting in high-porosity sandstone, Bassin du Sud-Est, Provence, France. J. Struct. Geol. 32, 1590–1608.
Sammis, C., King, G., Biegel, R., 1987. The kinematics of gouge deformation. Pure Appl. Geophys. 125 (5), 777–812.
Schild, M., Siegesmund, S., Vollbrecht, A., Mazurek, M., 2000. Characterisation of granite matrix porosity and pore-space geometry by *in-situ* and laboratory methods. Geophys. J. Int. 146, 111–125.
Schmitt, M., Halisch, M., Müller, C., Fernandes, C.P., 2016. Classification and quantification of pore shapes in sandstone reservoir rocks with 3-D X-ray microcomputed tomography. Solid Earth 7 (1), 285–300.
Schneider, C.A., Rasband, W.S., Eliceiri, K.W., 2012. NIH Image to ImageJ: 25 years of image analysis. Nat. Methods 9, 671–675.
Scholz, C., Molnar, P., Johnson, T., 1972. Detailed studies of frictional sliding of granite and implications for the earthquake mechanism. J. Geophys. Res. 77 (32), 6392–6406.
Scott, Thurman E., Nielsen, K.C., 1991. The effects of porosity on the brittle-ductile transition in sandstones. J. Geophys. Res. Solid Earth 96 (B1), 405–414.
Shimamoto, T., Logan, J.M., 1981. Effects of simulated clay gouges on the sliding behavior of Tennessee sandston. Tectonophysics 75 (3), 243–255.
Shipton, Z.K., Cowie, P.A., 2001. Damage zone and slip-surface evolution over μm to km scales in high-porosity Navajo sandstone, Utah. J. Struct. Geol. 23 (12), 1825–1844.
Shipton, Z.K., Evans, J.P., Thompson, L.B., 2005. The Geometry and Thickness of Deformation-band Fault Core and its Influence on Sealing Characteristics of Deformation-band Fault Zones.
Takemura, T., Golshani, A., Oda, M., Suzuki, K., 2003. Preferred orientations of open microcracks in granite and their relation with anisotropic elasticity. Int. J. Rock Mech. Min. Sci. 40, 443–454.
Tanikawa, W., Shimamoto, T., 2009. Comparison of Klinkenberg-corrected gas permeability and water permeability in sedimentary rocks. Int. J. Rock Mech. Min. Sci. 46, 229–238.
Taylor, J.M., 1950. Pore-space reduction in sandstones. AAPG Bull. 34 (4), 701–716.
Torabi, A., Fossen, H., 2009. Spatial variation of microstructure and petrophysical properties along deformation bands in reservoir sandstones. AAPG Bull. 93, 919–938.
Walker, G., Burley, S., 1991. Luminescence petrography and spectroscopic studies of diagenetic minerals. In luminescence microscopy and spectroscopy: quantitative and qualitative applications. SEPM Short. Course 25, 83–96.
Walsh, J.B., Brace, W.F., 1984. The effect of pressure on porosity and the transport properties of rock. J. Geophys. Res. 9425–9431, 89–B11.
Youd, T.L., 1972. Compaction of sands by repeated shear straining. J. Soil Mech. Found. Div. 98 (7), 709–725.
Zhang, J.J., Bentley, L.R., 2003. CREWES Research Report. Pore Geometry and Elastic Moduli in Sandstones, vol. 15.
Zhu, W., Wong, T.F., 1997. The transition from brittle faulting to cataclastic flow: permeability evolution. J. Geophys. Res. Solid Earth 102 (B2), 3027–3041.